KUOPION YLIOPISTON JULKAISUJA C. LUONNONTIETEET JA YMPÄRISTÖTIETEET 212
KUOPIO UNIVERSITY PUBLICATIONS C. NATURAL AND ENVIRONMENTAL SCIENCES 212

OLLI-PEKKA TOSSAVAINEN

Shape Estimation in Electrical Impedance Tomography

Doctoral dissertation

To be presented by permission of the Faculty of Natural and Environmental Sciences
of the University of Kuopio for public examination in Auditorium L22,
Snellmania building, University of Kuopio,
on Friday 18th May 2007, at 12 noon

Department of Physics
University of Kuopio

KUOPION YLIOPISTO

KUOPIO 2007

Distributor: Kuopio University Library
P.O. Box 1627
FI-70211 KUOPIO
FINLAND
Tel. +358 17 163 430
Fax +358 17 163 410
http://www.uku.fi/kirjasto/julkaisutoiminta/julkmyyn.html

Series Editors: Professor Pertti Pasanen, Ph.D.
Department of Environmental Sciences

Professor Jari Kaipio, Ph.D.
Department of Physics

Author's address: Department of Physics
University of Kuopio
P.O. Box 1627
FI-70211 KUOPIO
FINLAND
Tel. +358 17 162 371
Fax +358 17 162 373
E-mail: Olli-Pekka.Tossavainen@uku.fi

Supervisors: Docent Marko Vauhkonen, Ph.D.
Department of Physics
University of Kuopio

Docent Ville Kolehmainen, Ph.D.
Department of Physics
University of Kuopio

Reviewers: Professor Simon Arridge, Ph.D.
Department of Computer Science
University College London
UK

Professor Sin Kim, Ph.D.
Department of Nuclear and Energy Engineering
Cheju National University, Cheju
Korea

Opponent: Professor Markku Kataja, Ph.D.
Department of Physics
University of Jyväskylä

ISBN 978-951-27-0690-7
ISBN 978-951-27-0785-0 (PDF)
ISSN 1235-0486

Kopijyvä
Kuopio 2007
Finland

Tossavainen, Olli-Pekka. Shape Estimation in Electrical Impedance Tomography. Kuopio University Publications C. Natural and Environmental Sciences 212. 2007. 64 p.
ISBN 978-951-27-0690-7
ISBN 978-951-27-0785-0 (PDF)
ISSN 1235-0486

ABSTRACT

Electrical impedance tomography (EIT) is an imaging modality which is used in medicine and industry to obtain information from inside the target. This thesis is focused on the industrial applications.

In EIT, currents are applied through an array of electrodes attached on the surface of the object and the resulting voltages are measured using the same electrodes. Based on these measurements an estimate for the internal admittivity distribution is computed. The image reconstruction in EIT is an ill-posed inverse problem.

The reconstruction in the tomographic imaging is usually made in a fixed pixel grid. However, if it is known that the object consists of a few separate subregions of different materials with constant admittivity values, one can employ so-called shape estimation methods. The use of shape estimation methods makes the inverse problem less ill-posed by using a small number of unknown parameters to describe the target.

In this thesis, novel shape estimation methods for EIT are proposed. The motivation for the methods stems from the industrial process tomography applications of EIT. More specifically, three different applications are considered. The first of these is the estimation of a free-surface between air and conductive liquid in industrial process pipeline. The second application is the estimation of the free-surface between oil and water in industrial process pipeline. The third application is sedimentation monitoring in a separation tank.

The free-surface is an open interface between two phases. In this thesis, the free-surface estimation methods are formulated as regularized output least squares problems. Two different computational methods are proposed for the estimation of the free-surface between air and liquid. One method is proposed for the estimation of the oil-water interface.

In sedimentation monitoring, a novel shape estimation method is proposed in which locations of two surfaces are estimated simultaneously. The proposed computational method is based on shape estimation and state estimation formulation of the EIT problem. Sedimentation is parameterized by the locations of the phase interfaces and conductivities of the phase layers.

The performance of the methods proposed in this thesis is evaluated using simulated data. Furthermore, one air-liquid interface estimation method and the three-dimensional sedimentation monitoring model are evaluated using experimental data. The results indicate that the methods developed in this thesis have a promising performance.

AMS (MOS) Classification: 35R30, 35R35, 74S05
PACS Classification: 42.30.Wb
Universal Decimal Classification: 519.632
INSPEC Thesaurus: electric impedance imaging; inverse problems; image reconstruction; electrical conductivity; finite element analysis; sedimentation; Kalman filters; process monitoring

Acknowledgements

This work was carried out in the Department of Physics at the University of Kuopio during the years 2003–2007.

I am very grateful to my supervisors and co-authors Docent Marko Vauhkonen, Ph.D., and Docent Ville Kolehmainen, Ph.D., for the privilege of having the excellent guidance and their constant support during this work. I also wish to express my warmest gratitude to my co-authors Professor Sin Kim, Ph.D., Lasse Heikkinen, Ph.D., and Tuomo Savolainen M.Sc., for the fruitful collaboration and discussions during this work.

I want to thank the official reviewers Professor Simon Arridge, Ph.D., and Professor Sin Kim, Ph.D., for carefully reading the manuscript and giving constructive criticism and valuable suggestions.

I want to thank Professor Jari Kaipio, Ph.D., for his encouragement and for the opportunity to work in the Department of Physics. I also wish to thank the staff of the Department of Physics at the University of Kuopio for their support.

I also want to thank the members of the Inverse Problems research group. Especially, I want to thank Janne Huttunen, Phil.Lic., for his friendship and for all help during these years. Many thanks to Anssi Lehikoinen, M.Sc. (tech.), for his friendship and fruitful collaboration during these years. Thanks to Jari Kourunen, M.Sc., for his assistance in EIT measurements.

Thanks to the members of the Biosignal Analysis and Medical Imaging research group for all their support.

I also want to thank my parents Arto and Eila, my sisters Marjo and Anne for their constant support.

Finally, I want to thank my dear wife Henna for her endless love and support.

Kuopio, 30th April 2007

Olli-Pekka Tossavainen

Abbreviations

2D	Two-dimensional
3D	Three-dimensional
CM	Conditional mean
ECT	Electrical capacitance tomography
EIT	Electrical impedance tomography
EKF	Extended Kalman filter
ERT	Electrical resistance tomography
FE	Finite element
FEM	Finite element method
G–N	Gauss–Newton
LS	Least squares
MAP	Maximum a posteriori
ML	Maximum likelihood
ROLS	Regularized output least squares

Notations

$(\cdot)^{\mathrm{T}}$	Transpose
$\widehat{(\cdot)}$	Complex conjugate
$(\cdot)_{\mathrm{re}}$	Real part
$(\cdot)_{\mathrm{im}}$	Imaginary part
$\|\cdot\|$	Euclidean norm
A	EIT system matrix
α	Regularization parameter
B, C, D	Blocks of the system matrix A
b	Finite element solution vector
$\mathcal{C}$	Free-surface, phase interface
D_t	Noise transition matrix
$\varepsilon, \varepsilon_t$	Observation noise
ϵ	Permittivity
η	Admittivity
e_l	lth electrode
$E\{\cdot\}$	Expectation operator
F_t	State transition / evolution matrix
Γ	Covariance matrix
γ, γ_t	Shape parameter vector
$I^{(k)}$	kth current pattern
I_l	Injected current through lth electrode
J, J_t	Jacobian matrix
j	Imaginary unit
K_t	Kalman gain matrix
L_θ	Regularization matrix

λ	Lagrangian multiplier vector
$\mathcal{M}$	Measurement operator
N	Nodal coordinate vector
$\mathcal{N}$	Gaussian density
ν	Outward unit normal
Ω	Domain
$\partial\Omega$	Boundary of Ω
ω	Angular frequency
$\pi(\cdot)$	Probability density
s	Curve parameter $\in [0, 1]$
σ, σ_t	Conductivity
Φ	Lagrangian constraint
φ_i, n_j	Finite element basis function
r	Position vector
$\mathcal{S}_k$	kth subdomain
θ, θ_t	Parameter vector
θ^*	Expectation value of θ
$\theta_{t\|t-1}$	Expectation of prediction density
$\theta_{t\|t}$	Expectation of filtered density
$U(\theta), U_t(\theta_t)$	Forward model
U_l	lth electrode voltage
$U^{(k)}$	Electrode voltages w.r.t. kth current pattern
U_h	FEM approximation of electrode voltages
u	Potential distribution inside Ω
u_h	FEM approximation of u
V, V_t	Data vector
$v, \mathcal{V}$	FEM test function
w_t	State noise

LIST OF ORIGINAL PUBLICATIONS

This thesis consists of an overview and the following four original articles which are referred to in the text by their Roman numerals I–IV:

I O.-P. Tossavainen, M. Vauhkonen, L.M. Heikkinen, and T. Savolainen. Estimating shapes and free surfaces with electrical impedance tomography. *Measurement Science and Technology*, 15:1402–1411, 2004.

II O.-P. Tossavainen, V. Kolehmainen, and M. Vauhkonen. Free-surface and admittivity estimation in electrical impedance tomography. *International Journal for Numerical Methods in Engineering*, 66:1991–2013, 2006.

III O.-P. Tossavainen, M. Vauhkonen, V. Kolehmainen, and K.Y. Kim. Tracking of moving interfaces in sedimentation processes using electrical impedance tomography. *Chemical Engineering Science*, 61:7717–7729, 2006.

IV O.-P. Tossavainen, M. Vauhkonen, and V. Kolehmainen. A three-dimensional shape estimation approach for tracking of phase interfaces in sedimentation processes using electrical impedance tomography. *Measurement Science and Technology*, 18:1413–1424, 2007.

Contents

Chapter I

Introduction

Tomographic imaging modalities have traditionally been used in medical applications. Nowadays they are utilized also in the monitoring of industrial processes. The tomographic imaging is often referred to *process tomography* when it is used in industrial context. The earliest meetings in process tomography were arranged in the early 90's [1, 2, 3, 4]. Furthermore, there has been four world congresses in industrial process tomography since 1999 [5, 6, 7, 8]. Process tomography is a growing field of research and it has become a potential measurement tool when optimizing and controlling industrial processes.

This thesis concentrates on electrical impedance tomography (EIT). EIT is a diffuse imaging modality in which weak alternating currents are injected into the object via an array of electrodes at the surface of the object and the resulting voltages are measured using the same electrodes. The objective is to estimate the admittivity distribution inside the object based on these voltage measurements. In many cases, the admittivity distribution carries valuable information about the structural and functional properties of the monitored target. For example, in process imaging different concentrations of process chemicals posses contrast in admittivities.

The admittivity distribution inside the object is usually estimated in a local element basis that is obtained, for example, from pixel or finite element (FE) discretization. However, in many applications, the object is known to consist of a few separate subregions with constant but unknown admittivities, see for example Figure 1.1. In these situations, shape estimation techniques are a well suited framework for the reconstruction. In shape estimation methods, the aim is to estimate the shapes, locations and admittivities of the subregions.

In this thesis, novel shape estimation methods for electrical impedance tomography are presented. The motivation for the methods stems from the industrial applications of EIT. Shape estimation approaches are potential image reconstruction methods for EIT because they enable a significant reduction in the number of unknown parameters compared to the traditional (e.g. pixelbased) reconstruction methods.

Three different applications are considered:

1. Estimation of the shape of a free-surface between air and liquid. The free-

surface is an open interface between two phases in an industrial process pipeline. Two different methods for the estimation of the air-liquid interface are proposed.

2. Estimation of the shape of a free-surface between oil and water in an industrial process pipeline.

3. Sedimentation monitoring. The sedimentation process is modelled by a three-layer model. The unknowns in the shape estimation problem are the locations of two phase interfaces and the conductivities of three phases.

All the methods presented in this thesis are verified with simulated data and two of them with experimental data.

One design criteria for the estimation methods of this thesis is the robustness of the methods in situations where the number of measurements is small. The small number of available measurements may be a consequence of some electrodes being in contact with air or some other very insulating material. The proposed shape parameterizations of the object can be used in the image reconstruction with a small number of data.

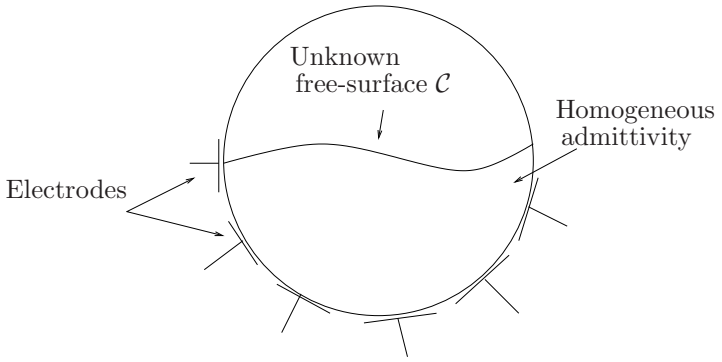

Figure 1.1: A schematic representation of a two-phase flow in an industrial pipe. Free-surface is denoted by $\mathcal{C}$. The free-surface is an open interface between two phases in an industrial process pipeline.

Contents of the thesis

This thesis is organized as follows. Chapter 2 presents a brief review on electrical impedance tomography and shape estimation methods in the context of EIT. Furthermore, a brief review on two-phase flow applications and sedimentation monitoring is given. In Chapter 3, the mathematical model of EIT is presented. Furthermore, a numerical solution for the mathematical model of EIT using the finite element method is presented and the data acquisition in EIT is briefly discussed. Chapter 4 discusses the inverse problem of EIT. The inverse problem is

defined and the commonly used reconstruction methods are reviewed. Furthermore, the shape estimation methods developed in this thesis are reviewed. In Chapter 5, the work is summarized. Conclusions and suggestions for the future extensions are given.

Chapter II

Background

2.1 Electrical impedance tomography

The history of electrical impedance tomography dates back to 1978 when Henderson and Webster described an "impedance camera" [55] for imaging the internal impedance of thorax. In 1980, Calderón formulated the problem of determining the internal conductivity distribution based on the electrical measurements made on the boundary [32]. This conjecture addressed by Calderón induced the start of research in both theoretical and practical aspects of EIT. In 1987, Sylvester and Uhlmann [112] solved Calderón's problem for conductivities with two derivatives in $\mathbb{R}^n$, $n \geq 3$. An important result in theoretical field of EIT was published by Nachman [92]. He proved global uniqueness in $\mathbb{R}^2$ for conductivities with two derivatives. In 2003, Astala and Päivärinta [17] proved Calderón's original conjecture which stated that a bounded measurable conductivity can be determined from boundary measurements in $\mathbb{R}^2$. Nowadays EIT has a variety of applications in medical [123, 28, 90, 88], industrial [127, 126] and geophysical [22, 74, 108, 67, 66] field.

In electrical impedance tomography, the aim is to reconstruct the admittivity distribution inside the object based on the electrical measurements made on the boundary of the object. In an EIT experiment, low amplitude alternating currents I_l are injected to the object Ω through the electrodes e_l attached on the boundary $\partial\Omega$ of the object and the resulting (complex valued) voltages U_l are measured using the same electrodes. Based on these voltage data, an estimate for the internal admittivity distribution η is computed.

In order to reconstruct the admittivity distribution inside the object Ω, that is, solve the *inverse problem* of EIT, a mathematical model that describes the observations is needed. Many different mathematical models for EIT exists but the most successful of these has been the *complete electrode model* (CEM) that is reviewed in Section 3.1.

The image reconstruction in electrical impedance tomography is an ill-posed[1] inverse problem. Moreover, the solution is very sensitive to the modelling errors.

[1] Ill-posed means that even arbitrary small changes in the data can cause large changes into the solution of the problem, i.e., the problem is unstable or has no unique solution.

Due to this nature, the solution of the EIT problem necessitates that the model for the measurements is accurate. Furthermore, due to the ill-posedness of the problem the problem has to be regularized. In regularization, the ill-posed inverse problem is replaced with a well-posed approximation of the inverse problem. A few examples of traditional regularization methods are the use of truncated singular value decomposition and truncated iterations. In this thesis, Tikhonov regularization is used. It is a versatile class of regularization methods which allows one to include knowledge of properties of the object into the inverse problem. An extensive review of regularization methods can be found in [71].

2.2 Shape estimation

2.2.1 Shape estimation in inverse problems

Shape estimation has been widely used for example in designing optimal wings for aeroplanes. In these situations, shape estimation is often referred to *shape optimization*. The optimization is done based on certain criteria and constraints. For example, the shapes of the wings and ship hulls have been optimized for minimum drag etc. For references of shape optimization, see [48, 86, 13, 12, 49].

This thesis is discusses shape estimation approaches in the context of the inverse problem of EIT. In shape estimation techniques, the reconstruction is defined in terms of the shapes of the subregion boundaries. Usually the boundaries are represented by parameterized curves and the reconstruction is stated as a problem of estimating the shape parameters given the data. With a shape parameterization, one typically has less unknown parameters compared to the traditional pixelwise parameterization. This leads potentially to a less ill-posed estimation problem. Different shape estimation methods for inverse problems have been previously examined, for example, in [33, 31, 14, 23, 10, 72, 80, 81].

In this thesis, the estimation methods for recovery of the shapes and locations of open surfaces are considered. More specifically, the practical applications are free-surface estimation and sedimentation monitoring. It is noted that the shape estimation methods in [80, 81, 75, 18], as well as the other traditional shape estimation methods have been developed for the recovery of closed boundaries of subregions that are embedded in the object domain. Therefore, they are not directly applicable for the shape estimation problems considered in this thesis.

2.2.2 Free-surface problem

The free-surface problem is related to the monitoring of two-phase flows. The free-surface is defined as an open interface between two phases, see Figure 1.1. In the literature, these phases are often referred to as *flow regimes*. Two-phase flow monitoring is important in many areas of industry. For example, in the oil industry one wants to determine which portion of the pipe is filled with gas or water and which portion is filled with oil. Based on the information obtained from the flow monitoring, the oil feed into the trunks can be optimized [45, 44]. Furthermore, this reduces the need of oil/gas/water separation. Another example of the free-

surface imaging can be found from the pneumatic water conveying systems. In these systems, the pipe may be only partially filled with water and above the water there is a void region (air). Then the aim is to find the shape of the void region, also referred to as *air slug* [42, 41].

Different methods have been developed for identifying the flow regimes. In direct measurement techniques, the flow regimes are recovered directly from the measurements, for example photographs. The use of high-speed photography in the flow regime identification has been examined in [37, 100]. The flow regimes are determined from photographs by interpreting them, for example, visually and/or statistically. Another way to identify the flow regimes is to use indirect techniques. For example, capacitance and impedance sensors are attached on the surface of the pipes and they are used to measure fraction of air in the pipe, see for example [9, 113, 21]. Furthermore, X-ray techniques to determine flow regimes have been used in [65].

Attractive techniques to identify two-phase flow regimes are the methods based on electrical tomographic imaging. For example, electrical capacitance tomography (ECT) has been used to monitor two-phase flows in [93, 63, 61]. ECT is closely related to EIT and electrical resistance tomography (ERT). In ERT, the capacitive effects are not taken into account, whereas in ECT, the aim is to reconstruct only the permittivity (capacitivity) distribution. The use of ERT in flow monitoring has been investigated for example in [41, 42, 95].

In this thesis, the identification of the flow regimes is done by estimating the location and shape of the free-surface between two flow regimes in an industrial pipeline using electrical impedance tomography. A simple application in which the justification of the shape estimation methods can be seen is presented in Figure 2.1. Figure 2.1 represents a very simple image reconstruction problem. The target (left subfigure) is a homogeneous conductivity distribution. The voltage measurements and the current injections are made from the right and left side of the object. However, the upper boundary of the object is curved and this fact is not taken into account in traditional pixelbased image reconstruction. As can be seen, the reconstructed pixelbased image (right subfigure) is severely erroneous. In shape estimation methods, the shape of the upper boundary and the conductivity of the target can be estimated simultaneously. There has also been studies in which the anisotropy is used to tackle the mismodelling of the geometry of the object in tomographic imaging, see [54, 82].

In this thesis, two different situations for the free-surface estimation are considered:

1. recovery of the shape of air-liquid interface and

2. recovery of the shape of oil-water interface.

It is noted that the problem of monitoring a pipeline filled only partially with liquid is especially challenging one. This due to the fact that there is no current passing into the non-conducting air slug. In computational terms this means that the mathematical models of EIT are not even valid in the air slug, and thus the

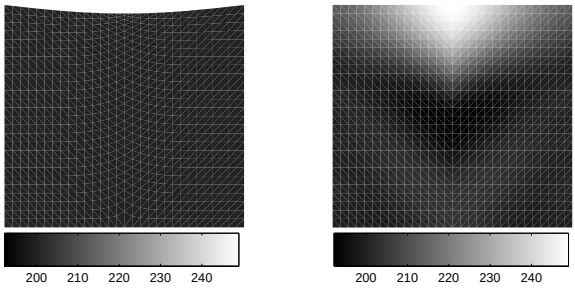

Figure 2.1: Effects of the boundary shape on the reconstructed resistivity (inverse of conductivity) distribution. Homogeneous resistivity distribution with deformed boundary shape (left) and reconstructed image when the boundary shape is wrong (right).

unknown free-surface should be treated as part of the exterior boundary of the computational domain. The methods developed in Publications I and II consider the free-surface problems in aforementioned situations.

2.2.3 Sedimentation monitoring

In sedimentation, a solid-fluid suspension is separated into its solid and fluid components under the influence of gravity [29]. It is an important process which is widely used in mining, waste water treatment, pulp and paper and in many other industrial processes. Information obtained from the monitoring of sedimentation can be utilized to control and optimize the sedimentation processes [129, 87].

In this thesis, a typical three-layer model for the sedimentation is used. In three-layer model, it is assumed that the fluids settle to three horizontal phase layers having sharp interfaces between the layers, see Figure 2.2. The top phase $\mathcal{S}_3$ is clear liquid, the middle phase $\mathcal{S}_2$ is a dilute slurry where the actual sedimentation takes place and the bottom phase $\mathcal{S}_1$ is a compact layer where hindered settling occurs [124, 30].

Sedimentation is usually characterized using the so-called settling curves $\gamma_q(t)$, $q = 1, 2$. In the settling curves, the time evolutions of the solid-liquid interfaces are presented. Another interesting quantity is the settling velocity $\dot{\gamma}_q(t)$ which is the velocity of the interface during the sedimentation process.

Different types of measurement techniques have been developed for determination of the settling curves and velocities. One example are light-based methods which are based on the optical properties of suspensions [97]. These methods typically use a laser source and photo-diodes as receivers. The optical measurements carry information about the solid concentration along the line between the laser

source and the receiver. Another example are automated methods based on image processing techniques such as edge detection, see [129, 130]. In these approaches, a large number of photographs of the tank are taken and image processing techniques are used to obtain the settling curves and velocities.

In electrical methods, the sedimentation is considered as three layers with different electric properties and non-invasive electromagnetic measurements that are made at the surface of the sedimentation tank are used for the estimation of the settling curves and velocities [39, 24, 121, 114, 101]. Instead of permanently attached metal electrodes, the use of linear sensor arrays in monitoring separation processes have been investigated in [26, 64, 91]. A common benefit of the electrical methods is that no transparent sedimentation tanks or settling columns are needed. In addition, unlike the light based methods, electrical methods require no extra models for the recovery of material parameters such as conductivity.

In this thesis, the monitoring of sedimentation processes using a electrical impedance tomography system is considered. A schematic illustration of the measurement setup and sedimentation model is shown in Figure 2.2. The proposed method utilizes shape estimation parameterization of the EIT problem and the state estimation paradigm. The details of the methods and employed measurement paradigms are presented in Publications III and IV.

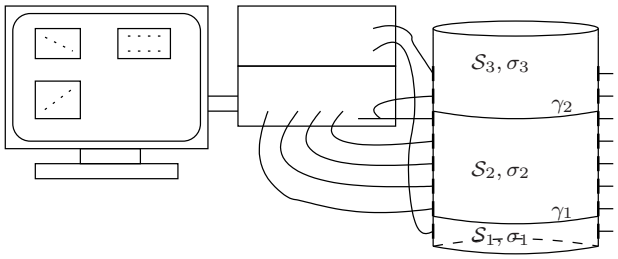

Figure 2.2: A schematic representation of sedimentation monitoring using the EIT system. The measurement electrodes are denoted by black surface patches on the sides of the sedimentation tank. $\mathcal{S}_k$ denotes the kth phase layer (subregion) in the sedimentation and σ_k denotes the conductivity of the kth phase. γ_q denotes the location of the qth phase interface.

Chapter III

Forward problem

In this chapter, the mathematical model of EIT and its numerical solution are reviewed. Furthermore, the data acquisition in EIT is briefly discussed.

3.1 The complete electrode model

In this thesis, the so-called complete electrode model is used as mathematical model for the EIT measurements. The model was originally proposed in [35]. The discussion in this section is mainly based on the references [111, 115, 50].

The complete electrode model is derived using complex valued admittivity η because some applications of this thesis use complex valued formulation of the model. Admittivity η can be expressed in terms of the conductivity σ and the permittivity ϵ as

$$\eta = \sigma + \mathrm{j}\omega\epsilon \ ,$$

where ω is the angular frequency of the injected current, j is the imaginary unit and the permittivity ϵ is

$$\epsilon = \epsilon_{\mathrm{r}}\epsilon_0 \ ,$$

where ϵ_{r} is the relative permittivity and ϵ_0 is the permittivity of empty space. Let $\Omega \subset \mathbb{R}^3$ denote the object domain. The behaviour of the electromagnetic fields in Ω is described with Maxwell's equations [40]. The equations can be written in the form

$$\nabla \times E = -\frac{\partial B}{\partial t} \ , \tag{3.1}$$

$$\nabla \times H = J + \frac{\partial D}{\partial t} \ , \tag{3.2}$$

where E is the electric field, H is the magnetic field, B is the magnetic induction, D is the electric displacement and J is the electric current density.

If the injected currents are time-harmonic with frequency ω, the electric and magnetic fields can be written in the form

$$E = E_0 \exp(\mathrm{j}\omega t) \ , \quad B = B_0 \exp(\mathrm{j}\omega t) \ .$$

In addition, if the domain Ω consists of linear and isotropic medium, the following relations are valid

$$D = \epsilon E \ , \tag{3.3}$$
$$B = \mu H \ , \tag{3.4}$$
$$J = \sigma E \ , \tag{3.5}$$

where μ is the permeability of the medium.

Using the relations (3.3–3.5) and by assuming that the injected currents are time-harmonic and cancelling out the oscillatory exponential, equations (3.1–3.2) can be written in the form

$$\nabla \times E = -\mathrm{j}\omega\mu H \ , \tag{3.6}$$
$$\nabla \times H = J + \mathrm{j}\omega\epsilon E \ . \tag{3.7}$$

Furthermore, the current density is divided into two components $J = J^o + J^s$ where $J^o = \sigma E$ is the so-called Ohmic current and J^s is the current source. Thus, equations (3.6–3.7) can be expressed in the form

$$\nabla \times E = -\mathrm{j}\omega\mu H \ , \tag{3.8}$$
$$\nabla \times H = (\sigma + \mathrm{j}\omega\epsilon)E + J^s \ . \tag{3.9}$$

These two equations are time-harmonic Maxwell's equations. In this case the frequency ω is fixed. Furthermore, in EIT some simplifications for these equations are made. In the frequency range used in EIT, the term $\omega\mu$ is small and, therefore, the term $-\mathrm{j}\omega\mu H$ is negligible. Using this assumption, equation (3.8) can be approximated as

$$\nabla \times E = 0 \ .$$

Since the curl of E is zero, there exists a gradient of the scalar potential ∇u such that

$$E = -\nabla u \ , \tag{3.10}$$

where u is the electric scalar potential. Furthermore, taking the divergence on both sides of equation (3.9) and substituting (3.10) into (3.9) yields

$$\nabla \cdot (\eta \nabla u) = 0 \quad \text{in } \Omega \ . \tag{3.11}$$

This approximation of the field equation is known as the quasi-static approximation. In equation (3.11), it has been set that $J^s = 0$ inside the domain. This is considered to be true in the frequency range used in EIT. Furthermore, the relation $\nabla \cdot \nabla \times H = 0$ was used.

If the capacitive effects are considered to be negligible, i.e., $\epsilon \approx 0$, the admittivity η can be approximated by the real valued conductivity σ.

Boundary conditions

There are a variety of boundary conditions that have been used for EIT. The most successful of these has been the complete electrode model, in which the boundary conditions take into account both the shunting effect of the electrodes and the contact impedances between the electrodes and the medium [35]. The boundary conditions for this model can be written as

$$u + z_l \eta \frac{\partial u}{\partial \nu} = U_l \quad \text{on } e_l,\ l = 1, 2, \ldots, L\ , \tag{3.12}$$

$$\int_{e_l} \eta \frac{\partial u}{\partial \nu}\, \mathrm{d}S = I_l \quad \text{on } e_l,\ l = 1, 2, \ldots, L\ , \tag{3.13}$$

$$\eta \frac{\partial u}{\partial \nu} = 0 \quad \text{on } \partial\Omega \setminus \bigcup_{l=1}^{L} e_l\ , \tag{3.14}$$

where e_l is the lth electrode, z_l is effective contact impedance between the lth electrode and medium, U_l are the voltages on the electrodes, I_l are the injected currents, ν is the outward unit normal and L denotes the number of electrodes. In addition, to ensure the existence and uniqueness of the solution u the following two conditions for the injected currents and measured voltages are needed. The vector $I = (I_1, \ldots, I_L)^{\mathrm{T}}$ has to satisfy the charge conservation law

$$\sum_{l=1}^{L} I_l = 0\ . \tag{3.15}$$

The vector I is called a *current pattern*. The ground voltage is chosen such that

$$\sum_{l=1}^{L} U_l = 0\ . \tag{3.16}$$

The vector $U = (U_1, \ldots, U_L)^{\mathrm{T}}$ is called a *voltage pattern*.

The solution of CEM consists of the electric potential distribution u inside Ω and the voltages U_l on the electrodes e_l.

3.2 Finite element solution of the complete electrode model

In this thesis, the numerical solution of the complete electrode model (3.11–3.16) is based on the finite element method. The following FEM approximation for the model has been derived in [118].

The construction of the FEM approximation begins with the variational formulation of the problem. It has been shown in [111] that the complete electrode model (3.11–3.16) has a (weak) solution $(u, U),\ u \in H^1(\Omega),\ U \in \mathbb{C}^L$, such that

$$\mathcal{B}_\eta((u, U), (v, \mathcal{V})) = \sum_{l=1}^{L} I_l \widehat{\mathcal{V}}_l\ , \forall v \in H^1(\Omega), \mathcal{V} \in \mathbb{C}^L,$$

where $\widehat{\mathcal{V}}$ is the complex conjugate of $\mathcal{V}$ and $\mathcal{B}_\eta$ is of the form

$$\mathcal{B}_\eta((u,U),(v,\mathcal{V})) = \int_\Omega (\sigma + \mathrm{j}\omega\epsilon)\nabla u \cdot \nabla \widehat{v}\ \mathrm{d}r + \sum_{l=1}^{L} \frac{1}{z_l} \int_{e_l} (u - U_l)(\widehat{v} - \widehat{\mathcal{V}}_l)\ \mathrm{d}S \quad (3.17)$$

and $H^1(\Omega)$ is the Sobolev space. In the FEM discretization, the domain Ω is divided into a mesh of disjoint elements and the solution of (3.17) is approximated by a finite dimensional approximation u_h of the form

$$u_\mathrm{h} = \sum_{i=1}^{N} \beta_i \varphi_i\ , \quad (3.18)$$

where N is the number of nodes in the FE mesh, φ_i are the (piecewise linear) nodal basis functions of the mesh and $\beta = (\beta_1, \ldots, \beta_N)^\mathrm{T} \in \mathbb{C}^N$. The coefficients β_i give the finite element solution u_h in the nodes.

For the voltages U on the electrodes, the approximation

$$U_\mathrm{h} = \sum_{j=1}^{L-1} \xi_j n_j = \mathcal{D}\xi \quad (3.19)$$

is used, where $n_1 = (1, -1, 0, \ldots, 0)^\mathrm{T}$, $n_2 = (1, 0, -1, 0, \ldots, 0)^\mathrm{T} \in \mathbb{R}^L$, etc. and $\xi = (\xi_1, \ldots, \xi_{L-1})^\mathrm{T} \in \mathbb{C}^{L-1}$. The matrix $\mathcal{D}$ contains the vectors $n_1, \ldots, n_{L-1}$ as columns and the coefficients ξ_i give the referenced voltages on the electrodes. By substituting the approximations (3.18–3.19) into equation (3.17) and using the basis functions $\{\varphi_i\}$ and $\{n_j\}$ as the test functions, the matrix equation

$$Ab = \mathcal{F} \quad (3.20)$$

is obtained, where

$$b = \begin{pmatrix} \beta \\ \xi \end{pmatrix}\ .$$

The data vector $\mathcal{F}$ is of the form

$$\mathcal{F} = \begin{pmatrix} \mathbf{0} \\ \sum_{l=1}^{L} I_l (n_j)_l \end{pmatrix} = \begin{pmatrix} \mathbf{0} \\ \tilde{I} \end{pmatrix}\ ,$$

where $\mathbf{0} = (0, \ldots, 0)^\mathrm{T} \in \mathbb{R}^N$, $\tilde{I} = (I_1 - I_2, I_1 - I_3, \ldots, I_1 - I_L)^\mathrm{T} \in \mathbb{C}^{L-1}$ and the notation $(n_j)_l$ refers to the lth component of vector n_j. The system matrix A is a complex valued $(N + L - 1) \times (N + L - 1)$ matrix of the form

$$A = \begin{pmatrix} B & C \\ C^\mathrm{T} & D \end{pmatrix}\ , \quad (3.21)$$

where

$$B(i,j) = \int_\Omega \eta \nabla\varphi_i \cdot \nabla\varphi_j \ \mathrm{d}r + \sum_{l=1}^{L} \frac{1}{z_l} \int_{e_l} \varphi_i \varphi_j \ \mathrm{d}S, \quad i,j = 1,2,\ldots,N \tag{3.22}$$

$$C(i,j) = -\left(\frac{1}{z_1} \int_{e_1} \varphi_i \ \mathrm{d}S - \frac{1}{z_{j+1}} \int_{e_{j+1}} \varphi_i \ \mathrm{d}S \right),$$
$$i = 1,2,\ldots,N \ , \ j = 1,2,\ldots,L-1$$

$$D(i,j) = \sum_{l=1}^{L} \frac{1}{z_l} \int_{e_l} (n_i)_l (n_j)_l \ \mathrm{d}S$$
$$= \begin{cases} \frac{|e_1|}{z_1}, & i \neq j \\ \frac{|e_1|}{z_1} + \frac{|e_{j+1}|}{z_{j+1}}, & i = j \end{cases} \ , \ i,j = 1,2,\ldots,L-1 \ ,$$

where $|e_j|$ is the measure (length in 2D, area in 3D) of the jth electrode. From (3.20) b can be solved formally as

$$b = A^{-1}\mathcal{F} \ . \tag{3.23}$$

In equation (3.23), the relation between the injected currents and the electrode voltages is of the form [119]

$$U_{\mathrm{h}}^{(k)} = R(\eta) I^{(k)} \ , \tag{3.24}$$

where $U_{\mathrm{h}}^{(k)} \in \mathbb{C}^L$, $R(\eta) = \mathcal{D}\widetilde{R}(\eta)\mathcal{D}^{\mathrm{T}}$ and $\widetilde{R}(\eta)$ is an $(L-1)\times(L-1)$ block of the inverse matrix A^{-1} and $I^{(k)} = (I_1, I_2, \ldots, I_L)^{\mathrm{T}}$ is the vector of injected currents. The vector $I^{(k)}$ is called the kth *current pattern*.

Solution with multiple current patterns; A measurement frame

The reconstruction of the admittivity distribution requires measurements corresponding to multiple current injection patterns. The voltage data set that is obtained when several currents are injected consecutively is called a *frame*. The complex valued equation (3.20) can be solved in real valued form using the following relations. Since A, b and $\mathcal{F}$ are complex valued, equation (3.20) can be written in form

$$\begin{aligned} (\mathcal{F}_{\mathrm{re}} + \mathrm{j}\mathcal{F}_{\mathrm{im}}) &= (A_{\mathrm{re}} + \mathrm{j}A_{\mathrm{im}})(b_{\mathrm{re}} + \mathrm{j}b_{\mathrm{im}}) \\ &= A_{\mathrm{re}}b_{\mathrm{re}} + \mathrm{j}A_{\mathrm{re}}b_{\mathrm{im}} + \mathrm{j}A_{\mathrm{im}}b_{\mathrm{re}} + \mathrm{j}^2 A_{\mathrm{im}}b_{\mathrm{im}} \\ &= A_{\mathrm{re}}b_{\mathrm{re}} - A_{\mathrm{im}}b_{\mathrm{im}} + \mathrm{j}(A_{\mathrm{re}}b_{\mathrm{im}} + A_{\mathrm{im}}b_{\mathrm{re}}) \ . \end{aligned}$$

This can be further written as a matrix–vector product as follows

$$\begin{pmatrix} A_{\mathrm{re}} & -A_{\mathrm{im}} \\ A_{\mathrm{im}} & A_{\mathrm{re}} \end{pmatrix} \begin{pmatrix} b_{\mathrm{re}} \\ b_{\mathrm{im}} \end{pmatrix} = \begin{pmatrix} \mathcal{F}_{\mathrm{re}} \\ \mathcal{F}_{\mathrm{im}} \end{pmatrix} \ . \tag{3.25}$$

From (3.25), it can be formally solved that

$$\begin{pmatrix} A_{\mathrm{re}} & -A_{\mathrm{im}} \\ A_{\mathrm{im}} & A_{\mathrm{re}} \end{pmatrix}^{-1} \begin{pmatrix} \mathcal{F}_{\mathrm{re}} \\ \mathcal{F}_{\mathrm{im}} \end{pmatrix} = \begin{pmatrix} b_{\mathrm{re}} \\ b_{\mathrm{im}} \end{pmatrix} . \tag{3.26}$$

In theory, it is possible to perform complex valued current injections. However, in this thesis the current injections are considered real valued. Thus, the imaginary parts of injected currents are zero. This corresponds to the assumption that the phase angle of the injected current is zero.

For the reconstruction, voltages U that would correspond the actual measurements are needed. Let $\mathcal{P}$ denote the matrix of measurement patterns. The matrix $\mathcal{P}$ maps the electrode potentials to voltage measurements made between different pairs of electrodes. The actual measurements with respect to the kth current pattern are obtained by multiplying $U_{\mathrm{h}}^{(k)}$ from the left with $\mathcal{P}$ such that

$$U^{(k)} = \mathcal{P}U_{\mathrm{h}}^{(k)} = \mathcal{P}\widetilde{\mathcal{D}}b^{(k)} = \mathcal{M}b^{(k)} ,$$

where

$$\widetilde{\mathcal{D}} = \begin{pmatrix} 0 & \mathcal{D} & 0 & 0 \\ 0 & 0 & 0 & \mathcal{D} \end{pmatrix}$$

and

$$\mathcal{P}\widetilde{\mathcal{D}} = \mathcal{M} . \tag{3.27}$$

In (3.27), $\mathcal{M}$ is a measurement operator that maps the solution of the FE system to the electrode measurements. The FE solution of the complete electrode model with known current injections and admittivity distribution is called the solution of the *forward problem of EIT*.

From equation (3.24) it can be seen that the dependence between the injected currents and the measured voltages is linear. However, the dependence between the voltages and the admittivity is nonlinear. This leads to a nonlinear inverse problem when solving the unknown admittivity. The inverse problem of EIT and the discretization of η are discussed in Chapter 4.

To complete the discussion of the numerical solution of CEM, the following notations are introduced. Let

$$U^{(k)}(\eta) = \mathcal{M}b^{(k)} \tag{3.28}$$

denote the vector of computed voltages for the kth current pattern $I^{(k)}$. Assuming that K current patterns are used in the EIT experiment, the measured voltage patterns $\{V^{(k)}\}_{k=1}^{K}$ and the set of computed voltages $\{U^{(k)}(\eta)\}_{k=1}^{K}$ are stacked to the vectors

$$V = \begin{pmatrix} V^{(1)} \\ \vdots \\ V^{(K)} \end{pmatrix} , \quad U(\eta) = \begin{pmatrix} U^{(1)}(\eta) \\ \vdots \\ U^{(K)}(\eta) \end{pmatrix} , \tag{3.29}$$

respectively. The total number of measurements is denoted by M, that is V and $U(\eta) \in \mathbb{R}^M$.

3.3 Data acquisition in EIT

In this section, a brief review on the current injection and voltage measurement schemes is given. Furthermore, EIT hardware that is needed for current injections and voltage measurements is discussed. The section is mainly based on reference [115].

3.3.1 Electrical impedance tomography hardware

A typical EIT system consists of one or more current generators, electrodes which are attached on the surface of the object, voltmeters, a control circuit and a computer in which the reconstruction algorithm processes the measured data. Furthermore, the visualization unit displays the reconstructed image. A schematic diagram of EIT hardware is presented in Figure 3.1.

The first reported electrical impedance tomography system was introduced in 1984 [20]. Later electrical impedance tomography systems have been designed by many research groups, see for example [110, 38]. Furthermore, a commercial EIT system was constructed in [62, 99]. The measurement systems which have been used in this thesis are called modular adaptive EIT systems and they have been built in the Department of Physics, University of Kuopio, Finland [104, 84]. The modularity means that the system is assembled from small modules. Thus, construction of the system can be altered between different measurement situations. The advantage of adaptability is that there is a minimal number of fixed parameters in the measurement system. For example, frequency, waveform and amplitude of injected currents can be easily changed by software. The EIT system presented in [104] consists of a main EIT unit and an additional multiplexer unit. The main EIT unit includes voltage waveform units, voltage-to-current converters, voltage measurement units, digital signal processing part and PC computer. With the use of multiplexer unit the number of the measurement and injection channels can be increased from the 16 channels of main unit up to 96 channels. The use of multiplexer unit reduces the cost of the system but as a drawback the measurement times become longer compared to 96 parallel measurement and injection channels. The novel KIT4 (Kuopio Impedance Tomography) system [84] has a total number of 16 injection channels and up to 80 parallel measurement channels.

3.3.2 Measurement strategies

In the EIT experiment, the measurements have to contain as much information on the admittivity distribution as possible. Hence, the selection of the measurement strategy is a crucial part of the EIT measurement system.

Current injections

The sensitivity of EIT depends on the current density within the object. There are two main strategies for the current injection and data collection in EIT. These are called *pair-drive* and *multiple-drive* methods.

In the pair-drive methods the current is applied between two electrodes and the voltages are measured using all the electrodes. This is the more commonly

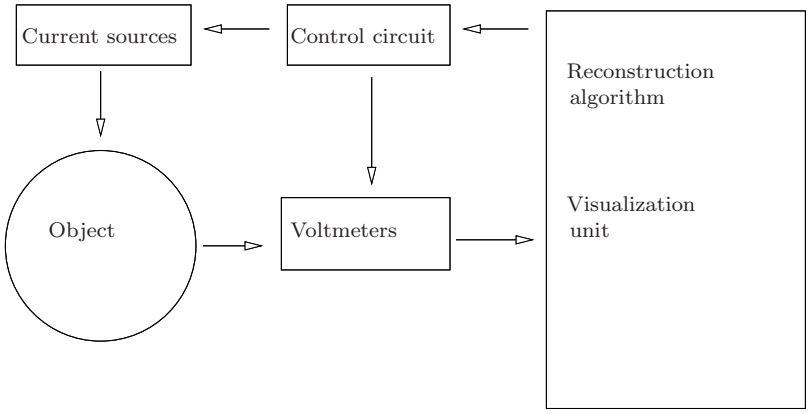

Figure 3.1: A schematic diagram of electrical impedance tomography measurement system [115].

used method because it provides simplicity in the injection system. The pair-drive methods include such protocols as *adjacent method* and *opposite method*, see for example [50].

In the multiple-drive methods all electrodes can be used simultaneously to inject currents. These methods produce the most uniform current density into the object [36]. As a drawback, they require as many current generators for one current injection as there are electrodes. This increases the complexity of the measurement system.

As an advantage, the multiple-drive methods can be used to maximize the information content of the measurements, i.e., distinguishability of two conductivity distributions. Distinguishability has been originally defined in [60] as follows. Two conductivity distributions σ_1 and σ_2 are distinguishable with measurement precision κ if there exists a current pattern $\|I\| = 1$ such that

$$\|R(\sigma_1)I - R(\sigma_2)I\| > \kappa \ . \tag{3.30}$$

Based on the definition (3.30), in articles [60, 47, 34] the authors defined the *optimal current pattern* to distinguish σ_1 from σ_2 as the current vector I which maximizes the distinguishability as follows

$$\max_I \frac{\|R(\sigma_1)I - R(\sigma_2)I\|}{\|I\|} \ .$$

For example in [60, 34] it was shown that in case of a centered rotation invariant annulus, the best distinguishability is obtained when a so-called *trigonometric current pattern* is used. For more information on optimal current patterns, see [69, 73].

Voltage measurements

The electrode voltages are measured with respect to some reference electrode. There are two possibilities to choose this electrode. The first possibility is to collect the data in such way that the voltages are measured differentially between the adjacent electrodes. This means that the reference electrode is changed for each measurement. The second way is to choose a fixed reference electrode for all the measurements.

Contact impedance

The EIT systems are mainly designed such that they inject currents and measure voltages instead of applying voltages and measuring currents [123]. This is due to the fact that there always exists a contact impedance between the electrode and object. Contact impedance has almost a negligible effect on the voltage measurements if there is no current passing through the electrodes during voltage measurement. When a largest possible number of measurements per current injection is preferred one has to measure voltages also from the current carrying (injecting) electrodes. It has been shown that the contact impedance value has its biggest effect on the reconstruction when measurements from current carrying electrodes are used [36]. Naturally, these measurements can be neglected in the case of pair-drive injections. However, in [36] it was also concluded that the measurements from the current carrying electrodes have the best information content about the conductivity distribution. Moreover, when using multiple-drive methods all the voltages are measured from current carrying electrodes.

In practise, the contact impedance values are determined from the EIT measurements. This can be done for example in the case of pair-drive method as follows. When the current injection protocol has been chosen, a reference voltage set is measured from the object having homogeneous conductivity. From these measurements, the following parameters are estimated: individual contact impedances for all current carrying electrodes, a common contact impedance value for the passive measurement electrodes, and a global homogeneous conductivity value. This reduces estimation errors in the image. For more information on the contact impedance estimation, see [122, 50].

Chapter IV

Inverse problem

In this chapter, the inverse problem in EIT is discussed. The chapter is based on the references [71, 79] and Publications I–IV.

In EIT, the inverse problem is to estimate the admittivity distribution given the voltage measurements on the boundary. Let θ denote the vector of the unknown admittivity parameters, i.e., the coefficients of the finite dimensional representation of η. In this thesis, the inverse problem of EIT is considered as a least squares (LS) problem

$$\min_{\theta} \|V - U(\theta)\|^2 \ ,$$

where $U(\theta)$ and V are the nonlinear forward operator and measured voltages in terms of Chapter 3, respectively. As mentioned in Section 3.3.2 the electrode contact impedances z_l could also be included to the parameter vector θ. However, in the following discussion it is assumed that the contact impedances are either known or estimated separately based on a reference voltage set.

The reconstruction of the admittivity distribution based on the boundary voltages is a nonlinear ill-posed inverse problem. Since the inverse problem suffers from ill-posedness, the LS solution is either non-unique or unstable. Due to this fact, the original ill-posed inverse problem has to be replaced with a well-posed approximation. A commonly used way to make the problem more well-posed is to use *regularization* techniques.

Traditionally inverse problems have been regularized using truncated singular value decompositions or truncated conjugate gradient iterations when solving the LS problem. A more versatile technique is to use Tikhonov regularization which is considered in the estimation methods of Publications I and II. In Tikhonov regularization, a penalizing (regularization) functional is used to modify the LS problem such that a stable solution exists. This functional is used to penalize unwanted properties of the solution. These properties can be, for example, large jumps. In other words, if large jumps are penalized it can be viewed as making a smoothness assumption of the solution. Another example of the regularization functional is the so-called total variation functional. The use of total variation regularization and anisotropic regularization functionals in the EIT inverse problem have been discussed in [79].

A novel approach for solving inverse problems is statistical inversion. The key idea in statistical inversion is to formulate the inverse problem in a well-posed statistical form which uses *a priori* information about the unknowns to compensate for the incomplete information in the data. Separate probability distribution models are constructed for the prior information and the measurement data. The complete solution of the inverse problem is obtained as the posterior probability distribution based on these models and the Bayes' formula. The prior can be spatial or temporal. In this thesis, temporal prior information is embedded in the estimation methods presented in Publications III and IV. The practical solution of the inverse problem can be obtained by computing point estimates and confidence estimates from the posterior distribution.

In addition to the regularization, the shape estimation approaches presented in this thesis provide also another way of reducing the ill-posedness of the problem. Namely, with the shape parameterization utilized in Publications I–IV the number of the unknown parameters can be reduced significantly compared to traditional pixel based images. The shape parameterization can be selected based on the properties of the target. For example, in many cases the number of phase interfaces in the target can be assumed to be known beforehand.

There has been a variety of different methods which have been proposed for solving the EIT image reconstruction problem. In this chapter, these methods are roughly divided into three categories, which are: difference methods, static reconstruction methods and time-dependent methods. In Sections 4.1–4.3, a brief review of these three image reconstruction categories in EIT is given. The shape estimation methods presented in Publications I and II are static reconstruction methods. In Publications III and IV, the time-dependent formulation is employed. The computation of the Jacobian matrix is presented in Section 4.4. Finally, the shape estimation approaches developed in this thesis are reviewed in Section 4.5.

4.1 Difference methods

In difference methods, it is assumed that the unknown admittivity distribution does not differ much from a known background distribution: The aim of these methods is to reconstruct a small anomaly $\delta\theta = \theta - \theta_{\mathrm{bg}}$ from the background (reference) parameters θ_{bg} based on a linear perturbation model of the form

$$\delta V = \mathcal{K}\delta\theta \ , \tag{4.1}$$

where $\delta V = V - V_{\mathrm{bg}}$ is the *difference* between two data vectors which are measured at θ and θ_{bg}. The matrix $\mathcal{K}$ may be, for example, the Jacobian of the forward map $U(\theta)$ evaluated at θ_{bg}.

The first attempts to reconstruct EIT images were made using a backprojection method [20, 103], which falls under the formalism of equation (4.1). The idea of backprojection method stems from CT and emission tomography, where it is widely used. However, in EIT the backprojection method does not use a *straight line strategy* in which the observations are backprojected along straight lines. Instead, in EIT the backprojection is done using isopotential curves. In CT and emission

tomography only the elements on that are on the straight line between the source and detector cause changes in the measured beam. In EIT the changes in all the elements of the object affect all the measurements.

The difference methods are often used to monitor functional properties of the target, see for example [51]. The goal is to image temporal and spatial changes in the admittivity distribution. The advantages of the difference methods are the following:

- The speed of the reconstruction. More specifically, the matrix $\mathcal{K}$ is computed beforehand and only once. When a new set of measurements is available, the reconstruction is obtained by a simple matrix vector product. Thus, in practise, the difference methods can produce as many images per second as the EIT device is able to acquire measurement frames.
- Another advantage is that the method is robust despite modelling errors (e.g. in electrode locations). Mismodelling causes systematic errors in the data and these artifacts are well removed when the difference data are used.

One drawback of the difference methods is that they cannot reconstruct absolute admittivity distributions.

4.2 Static reconstruction methods

In this section, static image reconstruction methods in EIT are discussed. At first, the regularized output least squares (ROLS) approach is reviewed in Section 4.2.1. The ROLS approach is used in Publications I and II. The ROLS approach has also a statistical interpretation under certain assumptions about the unknowns and measurement noise. This interpretation is discussed in Section 4.2.2.

4.2.1 Regularized output least squares approach

Most of the current attempts to obtain static reconstructions in EIT are based on the nonlinear LS formulation of the problem, see for example [118, 56, 125, 59, 128, 43, 98, 25, 96, 58]. A common feature to these approaches is that they are referred to as *iterative methods* for the reason that the formulation leads to the solution of the problem using iterative algorithms. There has also been studies in which *direct methods* for producing absolute images in EIT have been considered. For more information on the direct methods in EIT, [89] and [109] are referred to. The following discussion is mainly based on [71, 79, 119].

In the following it is assumed that the voltage observations V are corrupted by additive observation noise ε. The observation model for EIT is of the form

$$V = U(\theta) + \varepsilon \ . \tag{4.2}$$

The aim is to minimize the observation error norm in the LS sense. With the notations of equations (3.29) and (4.2) the least squares functional for the EIT inverse problem can be stated as

$$\Xi(\theta) = \|L_\varepsilon(V - U(\theta))\|^2 \ , \tag{4.3}$$

where L_ε is a weighting matrix. Due to the ill-posedness of the inverse problem, the functional has to be regularized. A classical way to regularize the EIT inverse problem is to use Tikhonov regularization. Thus, the ROLS functional

$$\Xi_\alpha(\theta) = \|L_\varepsilon(V - U(\theta))\|^2 + \alpha\|L_\theta(\theta - \theta^*)\|^2 \tag{4.4}$$

is introduced where α is the so-called regularization parameter, L_θ is the regularization matrix and θ^* is our prior guess of the unknown parameters. A typical choice for the regularization matrix L_θ in the EIT literature is either the identity matrix, scaled diagonal or an approximation for the first or second-order differential operator, see for example [59, 58, 27, 125]. When the differential operators are used, it is often referred to as making *smoothness assumptions* of the parameters θ. An extensive review on choosing regularization matrix and novel choices for the regularization functional in EIT are given in [79].

The ROLS functional in equation (4.4) is commonly minimized using gradient based iterative methods. In this thesis, Gauss–Newton method is used. The algorithm is derived in the following.

In this case $U(\theta) = (U^{(1)}(\theta), \ldots, U^{(K)}(\theta))^{\mathrm{T}}$ is nonlinear with respect to the parameters θ. Assume that U is Fréchet differentiable. Hence, $U(\theta)$ can be written such that

$$U(\theta) = U(\theta^{(0)}) + J(\theta^{(0)})(\theta - \theta^{(0)}) + \mathcal{O}(\|\theta - \theta^{(0)}\|^2) \ ,$$

where the term $\mathcal{O}(\|\theta - \theta^{(0)}\|^2)$ includes all the higher-order terms. Neglecting the higher-order terms, $U(\theta)$ can be approximated in the neighbourhood of some $\theta^{(0)}$ as

$$U(\theta) \approx U(\theta^{(0)}) + J(\theta^{(0)})(\theta - \theta^{(0)}) \ ,$$

where

$$\begin{aligned} J(\theta^{(0)}) &= \frac{\partial U}{\partial \theta}(\theta^{(0)}) \\ &= \begin{pmatrix} \frac{\partial U^{(1)}}{\partial \theta_1}(\theta^{(0)}) & \cdots & \frac{\partial U^{(1)}}{\partial \theta_P}(\theta^{(0)}) \\ \vdots & \ddots & \vdots \\ \frac{\partial U^{(K)}}{\partial \theta_1}(\theta^{(0)}) & \cdots & \frac{\partial U^{(K)}}{\partial \theta_P}(\theta^{(0)}) \end{pmatrix} \ , \end{aligned} \tag{4.5}$$

where P is the number of parameters. The aim is to estimate parameters θ recursively, such that the sequence of iterations is of the form

$$\theta^{(i+1)} = \theta^{(i)} + \delta\theta^{(i)} \ ,$$

where *the update* $\delta\theta^{(i)}$ has to be solved such that $\theta^{(i+1)}$ is the solution of the linearized problem in $\theta^{(i)}$. Using the linearization of $U(\theta)$, the ROLS functional (4.4) can be approximated as

$$\Xi_\alpha(\theta) = \|L_\varepsilon(V - (U(\theta^{(0)}) + J(\theta^{(0)})(\theta - \theta^{(0)}))\|^2 + \alpha\|L_\theta(\theta - \theta^*)\|^2 \ .$$

For the recursion the following substitutions are made

$$\begin{aligned} \theta^{(0)} &\leftarrow \theta^{(i)} \quad \text{and} \\ \theta &\leftarrow \theta^{(i+1)} , \end{aligned}$$

and thus

$$\Xi_\alpha(\theta^{(i+1)}) = \|L_\varepsilon(V - U(\theta^{(i)}) - J(\theta^{(i)})(\theta^{(i+1)} - \theta^{(i)}))\|^2 + \alpha\|L_\theta(\theta^{(i+1)} - \theta^*)\|^2$$

is obtained. Furthermore, the following substitution is made

$$\delta\theta^{(i)} \leftarrow \theta^{(i+1)} - \theta^{(i)}$$

and thus, the linearized ROLS functional can be written as

$$\Xi_\alpha(\theta^{(i+1)}) = \|L_\varepsilon(V - U(\theta^{(i)}) - J(\theta^{(i)})\delta\theta^{(i)})\|^2 + \alpha\|L_\theta(\delta\theta^{(i)} - (\theta^* - \theta^{(i)}))\|^2 . \quad (4.6)$$

The solution of the above problem is the requested update $\delta\theta^{(i)}$. In order to solve the problem (4.6), it is stacked into the equivalent form

$$\begin{aligned} \Xi_\alpha(\theta^{(i+1)}) &= \left\| \begin{pmatrix} L_\varepsilon J(\theta^{(i)}) \\ \sqrt{\alpha}L_\theta \end{pmatrix} \delta\theta^{(i)} - \begin{pmatrix} L_\varepsilon(V - U(\theta^{(i)})) \\ \sqrt{\alpha}L_\theta(\theta^* - \theta^{(i)}) \end{pmatrix} \right\|^2 \\ &= \|\tilde{J}_{(i)}\delta\theta^{(i)} - \tilde{U}_{(i)}\|^2 , \end{aligned} \quad (4.7)$$

where

$$\tilde{U}_{(i)} = \begin{pmatrix} L_\varepsilon(V - U(\theta^{(i)})) \\ \sqrt{\alpha}L_\theta(\theta^* - \theta^{(i)}) \end{pmatrix} \quad \text{and} \quad \tilde{J}_{(i)} = \begin{pmatrix} L_\varepsilon J(\theta^{(i)}) \\ \sqrt{\alpha}L_\theta \end{pmatrix} . \quad (4.8)$$

The LS estimate for $\delta\theta^{(i)}$ is obtained as follows

$$\begin{aligned} \delta\theta^{(i)}_{\text{LS}} &= (\tilde{J}^{\text{T}}_{(i)}\tilde{J}_{(i)})^{-1}\tilde{J}^{\text{T}}_{(i)}\tilde{U}_{(i)} \\ &= (J^{\text{T}}_{(i)}L^{\text{T}}_\varepsilon L_\varepsilon J_{(i)} + \alpha L^{\text{T}}_\theta L_\theta)^{-1}(J^{\text{T}}_{(i)}L^{\text{T}}_\varepsilon L_\varepsilon(V - U(\theta^{(i)})) + \alpha L^{\text{T}}_\theta L_\theta(\theta^* - \theta^{(i)})) , \end{aligned} \quad (4.9)$$

where $J_{(i)} := J(\theta^{(i)})$. Thus, for the iteration it can be written that

$$\begin{aligned} \theta^{(i+1)} = \theta^{(i)} &+ \lambda_{(i)}(J^{\text{T}}_{(i)}L^{\text{T}}_\varepsilon L_\varepsilon J_{(i)} + \alpha L^{\text{T}}_\theta L_\theta)^{-1} \\ &\times (J^{\text{T}}_{(i)}L^{\text{T}}_\varepsilon L_\varepsilon(V - U(\theta^{(i)})) + \alpha L^{\text{T}}_\theta L_\theta(\theta^* - \theta^{(i)})) , \end{aligned}$$

where $\lambda_{(i)}$ is a step size parameter which is used to control the convergence of the iteration. The step size parameter can be estimated for example using inexact line search type algorithms [94].

Usually, the inverse matrix

$$(\tilde{J}^{\text{T}}_{(i)}\tilde{J}_{(i)})^{-1} ,$$

in equation (4.9) is not computed but instead the update $\delta\theta^{(i)}_{\text{LS}}$ is solved directly from (4.7) using, for example, QR decomposition and the stacked matrices $\tilde{J}_{(i)}$ and $\tilde{U}_{(i)}$ in (4.8). However, in large dimensional problems the G–N iteration is very memory consuming, see for example [119]. These problems can be overcome by using GMRES or conjugate gradient iterations when solving the normal equations in G–N, see for example [105].

4.2.2 Statistical interpretation

In this section, the concept of statistical inversion is briefly addressed. The text of this section is mainly based on references [71, 53].

In statistical interpretation, all the parameters are modelled as random variables which depend on each other through models. The information on the parameter values is expressed by probability distributions. In the statistical framework, the solution of the inverse problem is the posterior probability distribution.

In the following, some basic ideas of the statistical approach in inverse problems are given. Let V denote the vector of measurements, and θ the parameter vector. The conditional probability density of the measurement V given θ is of form

$$\pi(V|\theta) = \frac{\pi(\theta, V)}{\pi(\theta)} \ , \ \text{where} \quad \pi(\theta) \neq 0 \ , \tag{4.10}$$

where $\pi(\theta, V)$ denotes the joint probability density of θ and V. The conditional probability of V is called the *likelihood function* because it expresses the likelihood of different measurement outcomes with θ given.

The conditional probability density of θ given the measurement data V is of form

$$\pi(\theta|V) = \frac{\pi(\theta, V)}{\pi(V)} \ , \ \text{where} \quad \pi(V) \neq 0 \ , \tag{4.11}$$

where $\pi(V) = \int \pi(\theta, V) \ \mathrm{d}\theta$ is the probability density of the measurement V. Combining equations (4.10) and (4.11), the conditional probability density of θ can be written as

$$\pi(\theta|V) = \frac{\pi(V|\theta)\pi(\theta)}{\pi(V)} \ . \tag{4.12}$$

The previous formula is known as the Bayes' theorem for inverse problems and $\pi(\theta|V)$ is called the *posterior density* of θ. The posterior density $\pi(\theta|V)$ is proportional to $\pi(V|\theta)\pi(\theta)$, that is,

$$\pi(\theta|V) \propto \pi(V|\theta)\pi(\theta) \ ,$$

where, the probability density $\pi(\theta)$ is called the *prior density*. This term expresses the knowledge about the unknown prior to the measurement.

The posterior density contains more information on the solution than just a single point estimate. However, for the purpose of practical inference the posterior is often visualized and inferred by computing single point estimates, and spread or interval estimates for the point estimates from the posterior.

A popular point estimate is the *conditional mean* (CM) of the unknown θ given the data V, defined as

$$\theta_{\mathrm{CM}} = E\{\theta|V\} = \int \theta\pi(\theta|V) \ \mathrm{d}\theta \ ,$$

provided that the integral exists. In nonlinear cases (e.g. EIT), the CM estimate is computed typically using Markov chain Monte Carlo methods, see for example [71, 79].

Perhaps the most popular statistical estimate is the *maximum a posteriori* (MAP) estimate. It is defined by

$$\theta_{\text{MAP}} = \arg\max_{\theta} \pi(\theta|V) \ . \tag{4.13}$$

The computation of the MAP estimate requires solution of an optimization problem. Typically, the search for the maximizer is done using iterative, gradient based methods. Later it is seen that in some cases the computational problem is the same as with the ROLS methods. Finally, the *maximum likelihood* (ML) estimate is defined as

$$\theta_{\text{ML}} = \arg\max_{\theta} \pi(V|\theta) \ .$$

The ML estimate answers the question "*Which value of the unknown is most likely to produce the measured data V ?*".

Additive noise and Gaussian assumptions

Often the noise is assumed to be additive and mutually independent of the unknown θ. Hence, the observation model can be written as

$$V = U(\theta) + \varepsilon \ .$$

Assume further that θ and ε are Gaussian variables with probability densities

$$\pi(\theta) \propto \exp\left(-\frac{1}{2}(\theta-\theta^*)^{\mathrm{T}}\Gamma_\theta^{-1}(\theta-\theta^*)\right)$$

and

$$\pi(\varepsilon) \propto \exp\left(-\frac{1}{2}(\varepsilon-\varepsilon^*)^{\mathrm{T}}\Gamma_\varepsilon^{-1}(\varepsilon-\varepsilon^*)\right) \ .$$

Based on the assumption that θ and ε are mutually independent, it can be shown [71] that the likelihood density $\pi(V|\theta)$ can be written as

$$\pi(V|\theta) \propto \exp\left(-\frac{1}{2}(V-U(\theta)-\varepsilon^*)^{\mathrm{T}}\Gamma_\varepsilon^{-1}(V-U(\theta)-\varepsilon^*)\right) \ .$$

By using this information and the Bayes' formula the posterior density $\pi(\theta|V)$ becomes

$$\pi(\theta|V) \propto \exp\left(-\frac{1}{2}Q(\theta)\right) \ ,$$

where Q is a quadratic functional such that

$$Q(\theta) = (\theta-\theta^*)^{\mathrm{T}}\Gamma_\theta^{-1}(\theta-\theta^*) + (V-U(\theta)-\varepsilon^*)^{\mathrm{T}}\Gamma_\varepsilon^{-1}(V-U(\theta)-\varepsilon^*) \ .$$

Based on the definition (4.13), the MAP estimate is obtained as follows

$$\theta_{\text{MAP}} = \arg\min_{\theta} Q(\theta) \ . \tag{4.14}$$

An interesting feature of the MAP estimate can be seen by letting L_ε and L_θ be the Cholesky factors of matrices Γ_ε^{-1} and Γ_θ^{-1}, that is, $L_\theta^{\mathrm{T}} L_\theta = \Gamma_\theta^{-1}$ and for L_ε, respectively. Namely, equation (4.14) can be written as

$$\begin{aligned}\theta_{\mathrm{MAP}} &= \arg\min_\theta \big\{ (L_\varepsilon(U(\theta) - V - \varepsilon^*))^{\mathrm{T}} (L_\varepsilon(U(\theta) - V - \varepsilon^*)) \\ &\quad + (L_\theta(\theta - \theta^*))^{\mathrm{T}} (L_\theta(\theta - \theta^*)) \big\} \\ &= \arg\min_\theta \left\{ \|L_\varepsilon(U(\theta) - V - \varepsilon^*)\|^2 + \|L_\theta(\theta - \theta^*)\|^2 \right\} \ . \end{aligned} \tag{4.15}$$

The criterion (4.15) is clearly of the same form as the Tikhonov regularized functional (4.4). Therefore, the ROLS estimation corresponds to the MAP estimation when Gaussian assumptions about parameters θ and observation noise ε are made. For example, in (4.4) it has been implicitly assumed that $\varepsilon^* = 0$.

Correspondingly, the maximum likelihood estimate with the Gaussian noise model can be written as a general LS estimate

$$\theta_{\mathrm{ML}} = \arg\max \pi(V|\theta) = \min_\theta \|L_\varepsilon(V - U(\theta) - \varepsilon^*)\|^2 \ .$$

The covariance structure of the observation noise ε is usually unknown. However, when experimental data are used, one can estimate the covariance structure Γ_ε for the corresponding measurement setup as is done in Publication IV. For another reference see [52]. Furthermore, a detailed discussion on prior densities and models can be found in reference [71].

4.3 Time-dependent methods

In this thesis, time-dependent methods refer to the time dependent formulation of the EIT problem. The general reference for this formulation is [71]. For more references of the time-dependent EIT problem, see [107, 115, 116, 83, 70, 68, 120, 106]. In these references, the EIT problem is stated as a state estimation problem.

Time-dependent methods are important because the applications in industry require the monitoring of temporal evolution of the admittivity distributions that may exhibit significant changes even within the time needed to measure one frame. In the time-dependent methods, the unknown parameters θ are considered as a time-dependent quantities.

Let vector θ denote the vector of the unknown state parameters. In the sequel, if θ has a Gaussian distribution it is expressed as $\theta \sim \mathcal{N}(\theta^*, \Gamma_\theta)$, and similarly for ε etc. The explicit form of the vector θ depends on the chosen parameterization of the problem. Within the discrete time state estimation framework, the parameters θ are considered as a multi-variate real-valued stochastic process which has an evolution equation of the Markov type

$$\theta_{t+1} = F_t \theta_t + D_t w_t, \quad w_t \sim \mathcal{N}(0, \Gamma_{w_t}) \ , \tag{4.16}$$

where F_t is the state transition matrix, w_t is the evolution noise process (assumed zero mean Gaussian with covariance Γ_{w_t}), D_t is the transition matrix of the noise process w_t and the subindices $t \in \mathcal{I} = \{1, 2, \ldots, n\}$ denote the discrete time indices.

Equation (4.16) can be used to embed *a priori* information or assumptions about the temporal behaviour of the state parameters into the estimation problem. It can be also viewed as temporal regularization of the estimation problem [106]. The explicit forms of the matrices F_t and D_t for the evolution models used in this study are presented in Section 4.5.3 and can be found from Publication III.

For the EIT measurements, the observation equation is of the form

$$V_t = U_t(\theta_t) + \varepsilon_t, \quad \varepsilon_t \sim \mathcal{N}(\varepsilon_t^*, \Gamma_{\varepsilon_t}) \ , \tag{4.17}$$

where V_t is the vector of voltages measured at time index t, ε_t is the measurement noise process and U_t denotes the FEM based forward model.

The evolution equation (4.16) and the observation equation (4.17) constitute the *state-space* representation of the imaging problem. In the usual formulation of the state estimation problem, the objective is to compute the conditional expectations

$$\theta_{t|\mathcal{J}} = E\{\theta_t | \{V_k, k \in \mathcal{J}\}\} \ ,$$

where $\mathcal{J} \subseteq \mathcal{I}$ is a subset of all measurements. Below, the usual notation $\theta_{t|k}$ for the estimate $\theta_{t|\mathcal{J}}$ with $\mathcal{J} = \{1, 2, \ldots, k\}$ is used. If $k < t$ or $k = t$ the problem of determining the estimate is called prediction and filtering, respectively. In the case of linear evolution and observation equations and Gaussian noise processes, the recursive Kalman filter algorithm can be used for determining the estimates for the conditional expectation $\theta_{t|t}$ and covariance $\Gamma_{t|t}$.

Extended Kalman filter

The Kalman filtering is effective because Gaussian densities remain Gaussian in linear transformations. Hence, the density updating is achieved by updating only the expectation and the covariance. However, in non-linear problems the Kalman filter is not applicable and the computation of the exact conditional expectations $\theta_{t|t}$ with sampling based Bayes filtering methods would be computationally very demanding. Suboptimal estimates in nonlinear cases can be obtained by writing linear approximations for non-linear evolution and/or observation equations and apply the Kalman filter algorithm to the linearized problem. This commonly used approach is called the extended Kalman filter (EKF) [11, 71].

The linearized approximation for the observation equation (4.17) is written as

$$V_t = U_t(\theta_*) + J_t(\theta_t - \theta_*) + \varepsilon_t \ , \quad \varepsilon_t \sim \mathcal{N}(\varepsilon_t^*, \Gamma_{\varepsilon_t}) \ , \tag{4.18}$$

where θ_* is the linearization point in the state space and the Jacobian of the forward problem is defined as

$$J_t = \frac{\partial U_t}{\partial \theta_t}(\theta_*) \ .$$

Assuming that the linearization of the forward model is performed at the current predictor estimate $\theta_* = \theta_{t|t-1}$, the EKF estimates $\theta_{t|t}$ can be obtained recursively by using the following equations (with initializations $\theta_{0|0}$ and $\Gamma_{0|0}$):

- Time update (prediction)

$$\theta_{t|t-1} = F_{t-1}\theta_{t-1|t-1} \tag{4.19}$$
$$\Gamma_{t|t-1} = F_{t-1}\Gamma_{t-1|t-1}F_{t-1} + D_{t-1}\Gamma_{w_{t-1}}D_{t-1} \ , \tag{4.20}$$

- measurement update (filtering)

$$K_t = \Gamma_{t|t-1}J_t^{\mathrm{T}}(J_t\Gamma_{t|t-1}J_t^{\mathrm{T}} + \Gamma_{\varepsilon_t})^{-1} \tag{4.21}$$
$$\theta_{t|t} = \theta_{t|t-1} + K_t(V_t - U_t(\theta_{t|t-1}) - \varepsilon_t^*) \tag{4.22}$$
$$\Gamma_{t|t} = (I - K_tJ_t)\Gamma_{t|t-1} \ . \tag{4.23}$$

In the EKF equations, the matrix K_t is the so-called Kalman gain matrix and, here, I denotes the identity matrix.

For the statistical interpretation of the extended Kalman filter, see [71].

4.4 Computation of the Jacobian matrix

Since the dependence between unknown admittivity and measured voltages is non-linear, the solution of the inverse problem often requires the computation of the Jacobian matrix J with respect to the unknown parameters. The Jacobian matrix consists of the first-derivatives of the calculated electrode voltages $U(\theta)$ with respect to the ith unknown parameter which is denoted by θ_i. The use of the general notation for the unknown parameter is justified because each of the Publications I–IV uses a different combination of unknown parameters. Hence, the derivation of the Jacobian is kept as general as it is possible.

In this thesis, the adjoint differentiation method is used [15]. At first, consider equation (3.26). The electrode voltages with respect to the kth current pattern can be extracted from (3.26) by applying a measurement operator $\mathcal{M}$ such that

$$U^{(k)}(\theta) = \mathcal{M}b^{(k)} \ . \tag{4.24}$$

For the Jacobian in (4.5), the derivatives

$$\frac{\partial U^{(k)}}{\partial \theta_i} = \frac{\partial(\mathcal{M}b^{(k)})}{\partial \theta_i} = \mathcal{M}\frac{\partial b^{(k)}}{\partial \theta_i} \tag{4.25}$$

need to be computed.

The procedure continues by differentiating equation (3.25) with respect to the parameter θ_i as follows

$$\frac{\partial(Ab^{(k)})}{\partial \theta_i} = \frac{\partial \mathcal{F}^{(k)}}{\partial \theta_i} = 0 \ . \tag{4.26}$$

The derivative $\partial\mathcal{F}^{(k)}/\partial\theta_i$ equals to zero because the vector $\mathcal{F}^{(k)}$ of injected currents does not depend on parameter θ_i. Therefore, equation (4.26) can be written as

$$\frac{\partial A}{\partial \theta_i}b^{(k)} + A\frac{\partial b^{(k)}}{\partial \theta_i} = 0 \ . \tag{4.27}$$

From equation (4.27), $\partial b^{(k)}/\partial\theta_i$ is solved formally such that

$$\frac{\partial b^{(k)}}{\partial \theta_i} = -A^{-1}\frac{\partial A}{\partial \theta_i}b^{(k)} \ . \tag{4.28}$$

Furthermore, by applying the measurement operator $\mathcal{M}$, equation (4.28) can be expressed as

$$\mathcal{M}\frac{\partial b^{(k)}}{\partial \theta_i} = -\mathcal{M}A^{-1}\frac{\partial A}{\partial \theta_i}b^{(k)} = -\left(A^{-1}\mathcal{M}^{\mathrm{T}}\right)^{\mathrm{T}}\frac{\partial A}{\partial \theta_i}b^{(k)} \ .$$

Let b_* denote the solution of the adjoint problem such that

$$b_* = A^{-1}\mathcal{M}^{\mathrm{T}} \ .$$

Hence, the derivative of the electrode voltages $U^{(k)}$ with respect to the θ_i is of the form

$$\frac{\partial U^{(k)}}{\partial \theta_i} = -b_*^{\mathrm{T}}\frac{\partial A}{\partial \theta_i}b^{(k)} \ . \tag{4.29}$$

To obtain the final derivative, the system matrix A in equation (3.25) is differentiated with respect to the problem specific parameter θ_i. The ith column of the Jacobian in (4.5) is obtained by applying equation (4.29) for all voltages $b^{(k)}$, $k = 1, \ldots, K$. The computation of $\partial A/\partial\theta_i$ for the methods in Publications I–IV is explained in the next section.

4.5 Review on the computational methods in I–IV

In this section, the shape estimation methods that are proposed in Publications I–IV are summarized. Each of the subsections consists of review on the shape parameterization and the formulation of the inverse problem. Application examples of the estimation methods with simulated and experimental data can be found in Publications I–IV.

4.5.1 Estimation of free-surfaces using nodal parameters I

The objective of the proposed method is to estimate the shape and location of the free-surface between non-conducting void region and liquid. The free-surface is a part of the computational domain boundary, see Figure 4.1. The void region is not modelled using finite elements because there is no current passing trough the free-surface. The motivation for this method stems from the monitoring of air-liquid interface in industrial process pipeline.

The inverse problem is solved by minimizing the ROLS functional

$$\|V - U(\theta)\|^2 + \alpha\|L_\theta(\theta - \theta^*)\|^2 \ ,$$

where α controls the magnitude of the regularization functional and L_θ is the regularization matrix. Two different shape parameterizations were tested.

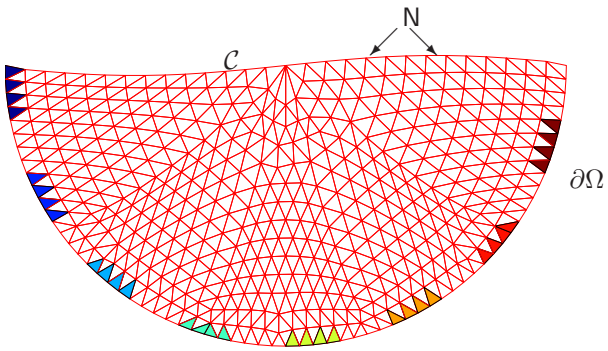

Figure 4.1: Example of the free-surface $\mathcal{C}$ between air and conductive liquid in a pipeline. The FE mesh describes the geometry of the conductive liquid. The nodes N on the upper boundary of the finite element mesh describe the free-surface $\mathcal{C}$. The coloured patches denote the locations of the electrodes.

Nodal coordinates as parameters

The unknown parameters are y-coordinates of the boundary nodes in the finite element mesh that define the free-surface, see Figure 4.1. In the reconstructions, the number of unknown nodal coordinates varied between 29 and 13 depending on the geometry. Furthermore, the global homogeneous conductivity value $\bar{\sigma}$ was estimated in experimental data reconstructions. Thus, the parameter vector was

$$\theta = (\mathsf{N}, \bar{\sigma})^{\mathrm{T}} \ ,$$

where N is the vector of the nodal y-coordinates. The regularization matrix L_θ was the second-order difference operator. The choice was based on the assumption that the free-surface is smooth.

The Jacobian matrix

$$J = \frac{\partial U}{\partial \mathsf{N}}$$

for the G–N iteration was computed using adjoint differentiation, equation (4.29). The derivative of the system matrix A with respect to the kth nodal coordinate N_k becomes

$$\frac{\partial A}{\partial \mathsf{N}_k} = \begin{pmatrix} \frac{\partial B}{\partial \mathsf{N}_k} & 0 \\ 0 & 0 \end{pmatrix} \ . \tag{4.30}$$

The elements of $\partial B/\partial \mathsf{N}_k$ in (4.30) are obtained as

$$\frac{\partial B(i,j)}{\partial \mathsf{N}_k} = \frac{\partial}{\partial \mathsf{N}_k} \int_\Omega \sigma \nabla \varphi_i \cdot \nabla \varphi_j \ \mathrm{d}r \ , \ i,j = 1,2,\ldots,N \ . \tag{4.31}$$

For more details about the evaluation of the derivative in (4.31), see Publication I.

The derivative of the system matrix A with respect to the conductivity is obtained as follows. At first, consider the conductivity in the element basis. The derivative with respect to conductivity of the eth element σ_e is obtained by noting that equation (3.22) can be written as [79]

$$B(i,j) = \sum_{e=1}^{E} \sigma_e K^{(e)}(i,j) + \sum_{l=1}^{L} \frac{1}{z_l} \int_{e_l} \varphi_i \varphi_j \, \mathrm{d}S \ , \quad i,j = 1,2,\ldots,N \ ,$$

where

$$K^{(e)}(i,j) = \int_{\Omega} \chi_e \nabla\varphi_i \cdot \nabla\varphi_j \, \mathrm{d}r \ ,$$

where χ_e is the characteristic function of eth element. By using these notations, the derivative $\partial A/\partial\sigma_e$ becomes

$$\frac{\partial A}{\partial \sigma_e} = \begin{pmatrix} K^{(e)} & 0 \\ 0 & 0 \end{pmatrix} \ . \tag{4.32}$$

The eth column for the Jacobian matrix is obtained by using equations (4.29) and (4.32). In order to compute the derivative with respect to the global conductivity $\bar{\sigma}$, that is,

$$\frac{\partial U^{(k)}}{\partial \bar{\sigma}} \ ,$$

the columns of the Jacobian matrix in (4.5) are summed. Note that in Publication I one simulated test case is presented in which the heterogeneous conductivity distribution σ is estimated simultaneously with the free-surface.

The performance of the nodal parameter approach was tested in various simulated test cases and with experimental data.

Control points of Bézier curve as parameters

In order to reduce the number of estimated parameters in contrast to nodal parameter approach, the unknown parameters are selected to be control points of a Bézier curve [102]

$$\mathcal{C}(s) = \begin{pmatrix} x(s) \\ y(s) \end{pmatrix} = \sum_{n=1}^{N_\Theta} \begin{pmatrix} \gamma_n^x \Theta_n^x(s) \\ \gamma_n^y \Theta_n^y(s) \end{pmatrix} , \quad s \in [0,1] \ , \tag{4.33}$$

where N_Θ is the number of control points γ_n^x, γ_n^y, and Θ_n^x and Θ_n^y are Bernstein basis functions, that is,

$$\Theta_n^x(s) = \Theta_n^y(s) = \binom{N_\Theta - 1}{n-1} s^{n-1} (1-s)^{N_\Theta - n}$$

with

$$\binom{N_\Theta - 1}{n-1} = \frac{(N_\Theta - 1)!}{(n-1)!(N_\Theta - n)!} \ .$$

The Bézier curve defines the shape and location of the free-surface. Via the Bézier curve, the nodal y-coordinates N representing the free-surface are controlled. In experimental data reconstructions the global homogeneous conductivity value $\bar{\sigma}$ was estimated with the locations of the control points. The parameter vector was

$$\theta = (\gamma(\mathsf{N}), \bar{\sigma})^{\mathrm{T}} \ ,$$

where γ contains the control points such that

$$\gamma = (\gamma_1^x, \ldots, \gamma_{N_\Theta}^x, \gamma_1^y, \ldots, \gamma_{N_\Theta}^y)^{\mathrm{T}} \ .$$

The regularization matrix L_θ was the first-order difference operator. The choice was based on the assumption that the consecutive control points are not far from each other. This resulted a relatively flat Bézier curve. The Jacobian matrix for the G–N iteration was computed using the chain rule of differentiation as follows

$$J = \frac{\partial U}{\partial \gamma_k} = \sum_p \frac{\partial U}{\partial \mathsf{N}_p} \frac{\partial \mathsf{N}_p}{\partial \gamma_k} \ ,$$

where the sum is calculated over all nodal parameters.

The performance of the Bézier curve approach was tested with the same simulated test cases and experimental data cases as the nodal parameter approach.

Discussion

Based on the results from simulations and tank experiments, the method seems promising. It is suggested that the proposed approach could be used in monitoring of air-liquid fraction inside the industrial pipeline.

The advantage of the proposed approach is that it is possible to estimate both the heterogeneous conductivity distribution and the shape of the unknown surface simultaneously. This was tested with a simulated test case. Furthermore, the Bézier curve approach reduced the number of unknown parameters more compared even to the nodal parameter approach.

One drawback of the proposed approach is that the nodes of the finite element mesh cannot be moved very far from their initial positions. Otherwise, the topology of the mesh will be broken and remeshing is required. To maintain the mesh quality, Laplacian smoothing [46] was applied to the mesh after each G–N iteration step. This increased computation times.

4.5.2 Free-surface and admittivity estimation II

The objective of this method is to estimate the shape and location of the free-surface $\mathcal{C}$

- between air and conductive liquid, and
- between oil and water.

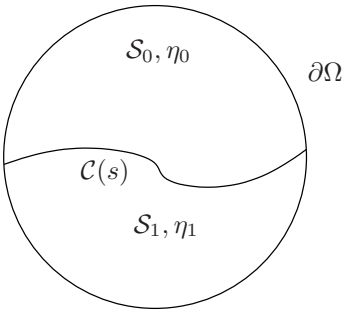

Figure 4.2: An example of a domain $\Omega = \cup_k \mathcal{S}_k$ with constant admittivities $\{\eta_k\},\ k = 0, 1$. The free-surface between subdomains $\mathcal{S}_0$ and $\mathcal{S}_1$ is denoted by $\mathcal{C}(s)$.

The motivation for this method stems from the monitoring of industrial pipelines in which two-phase flows are present.

In this method, the whole cross section of the pipe is modelled using finite element mesh. This leads to a situation in which mathematical model of EIT is not valid in the domain filled with air. However, in the proposed approach, this fact can be taken into account. The validity is ensured such that the material parameters which are numerically zero are approximated with a small positive constant. Hence, the validity of mathematical model in the whole object domain is guaranteed. It is shown in Publication II using simulation that this approximation is valid.

The shape estimation problem is formulated as follows. Let domain Ω be divided into two disjoint, simply connected subdomains $\mathcal{S}_k$

$$\Omega = \bigcup_{k=0}^{1} \mathcal{S}_k \ ,$$

which are separated by a smooth, open curve $\mathcal{C}(s)$ that has both ends at the boundary $\partial\Omega$. Let $s \in [0, 1]$ denote the curve parameter. For an illustration, see Figure 4.2. Further, assume that the subdomains $\{\mathcal{S}_k,\ k = 0, 1\}$ have constant, but unknown, admittivities $\{\eta_k\}$. The key point in the FEM implementation of this approach can be seen from the following. If χ_k denotes the characteristic function of subregion $\mathcal{S}_k$, the following can be written

$$\eta = \sum_{k=0}^{1} \eta_k \chi_k \ . \tag{4.34}$$

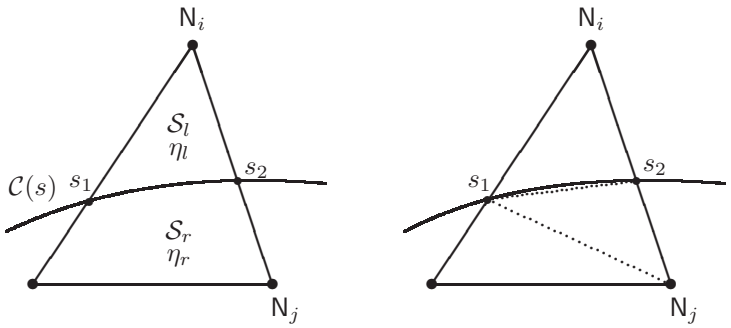

Figure 4.3: Left: A schematic representation of one FEM element Ω_m intercepted by the free-surface $\mathcal{C}(s)$. The value η_l corresponds to the value of the admittivity inside the region $\mathcal{S}_l$, and η_r is the value of the admittivity in the neighboring region $\mathcal{S}_r$, respectively. $\mathcal{C}(s_1)$ and $\mathcal{C}(s_2)$ are the intersection points of the boundary $\mathcal{C}(s)$ and the element edges. N_j and N_i are the nodal coordinates. Right: The division of the element Ω_m to three subtriangles.

By substituting equation (4.34) into (3.22) the elements of the block B in the FEM system matrix (3.21) are obtained as

$$B(i,j) = \sum_{k=0}^{1} \int_{\mathrm{supp}(\varphi_i\varphi_j)\cap\mathcal{S}_k} \eta_k \nabla\varphi_i \cdot \nabla\varphi_j \, \mathrm{d}r + \sum_{l=1}^{L} \frac{1}{z_l} \int_{e_l} \varphi_i\varphi_j \, \mathrm{d}S \;, \qquad (4.35)$$

where $\mathrm{supp}(\varphi_i\varphi_j)$ expresses the part of the domain Ω where both of the basis functions φ_i and φ_j are non-zero.

The free-surface $\mathcal{C}$ is parameterized using a Bézier curve. Since the free-surface lies inside the object domain, the FEM implementation of the forward model $U(\theta)$ is more challenging than in Publication I. The FEM implementation of $U(\theta)$ is based on the idea presented originally in reference [80]. The method employs subdivision of the triangle elements into the different regions when computing the integrals in equation (4.35). The elements are classified into two categories:

- If the free-surface intersects an element, the element is divided into two parts. Example is shown in Figure 4.3. Upper part belongs to the region $\mathcal{S}_l$, lower belongs to $\mathcal{S}_r$. In the computations, the part that belongs to $\mathcal{S}_r$ is divided into two subtriangles.
- If the element is not intersected, the integral over element can be computed directly using conventional FE techniques, see for example [57].

The inverse problem is stated as the ROLS problem augmented with the Lagrangian constraints. The constraints are used to prevent the first and last control

points of the Bézier curve from moving off from the domain boundary $\partial\Omega$. Thus, the minimized functional is written as

$$\frac{1}{2}\|U(\theta) - V\|^2 + \frac{\alpha}{2}\|L_\theta(\theta - \theta^*)\|^2 + \lambda^{\mathrm{T}}\Phi(\theta) \ ,$$

where $\lambda \in \mathbb{R}^2$ is the vector containing the Lagrangian multipliers. Thus, the number of constraints is two. The optimization procedure was carried out using the traditional Lagrange-multiplier-method and solving the Karush-Kuhn-Tucker-system (KKT-system) [94]. The first-order difference matrix was used for the regularization of the control points γ. The choice was based on the assumption that the consecutive control points are not far from each other. For the admittivities identity matrix was used as the regularization matrix.

The Jacobian matrix is computed using the adjoint differentiation (4.29). To obtain the derivative of the matrix A, the derivative of B with respect to the shape parameters needs to be computed. In reference [80], it was shown that using the notation of (4.33) the derivatives can be written as

$$\frac{\partial B(i,j)}{\partial \gamma_n^x} = \sum_{m|\Omega_m \in \mathcal{B}(\mathcal{C}) \cap \mathrm{supp}(\varphi_i \varphi_j)} (\eta_1 - \eta_0) \int_{s_1}^{s_2} \nabla\varphi_i \cdot \nabla\varphi_j \dot{y}(s) \Theta_n^x(s) \ \mathrm{d}s \ ,$$
$$i, j = 1, 2, \ldots, N \ ,$$

and

$$\frac{\partial B(i,j)}{\partial \gamma_n^y} = \sum_{m|\Omega_m \in \mathcal{B}(\mathcal{C}) \cap \mathrm{supp}(\varphi_i \varphi_j)} (\eta_0 - \eta_1) \int_{s_1}^{s_2} \nabla\varphi_i \cdot \nabla\varphi_j \dot{x}(s) \Theta_n^y(s) \ \mathrm{d}s \ ,$$
$$i, j = 1, 2, \ldots, N \ , \tag{4.36}$$

where $\dot{x}(s)$ and $\dot{y}(s)$ are the derivatives of the $x(s)$ and $y(s)$ with respect to s, respectively. The limits of integration s_1 and s_2 are the values of the curve parameter in the intersection points of the element edges and the curve $\mathcal{C}$ in each of the elements Ω_m. The element set $\mathcal{B}$ refers to the set of intersected elements.

By inspecting equation (3.22), it can be seen that the elements of the matrices $\partial B/\partial\sigma_k$ and $\partial B/\partial\epsilon_k$ are obtained as

$$\frac{\partial B(i,j)}{\partial \sigma_k} = \int_{\mathrm{supp}(\varphi_i \varphi_j) \cap \mathcal{S}_k} \nabla\varphi_i \cdot \nabla\varphi_j \ \mathrm{d}r \ , i, j = 1, 2, \ldots, N \ , \tag{4.37}$$

and

$$\frac{\partial B(i,j)}{\partial \epsilon_k} = \mathrm{j} \int_{\mathrm{supp}(\varphi_i \varphi_j) \cap S_k} \nabla\varphi_i \cdot \nabla\varphi_j \ \mathrm{d}r \ i, j = 1, 2, \ldots, N \ .$$

Air-liquid interface

In the reconstruction of air-liquid interface, the capacitive effects were not taken into account. For the G–N iteration, the initial level for the free-surface was chosen in the following way. The initial shape of the free-surface was assumed to

be flat. Furthermore, the y-coordinate of the surface was set into the middle of the topmost electrode that was in contact with liquid. Based on this initial guess for the free-surface location, the electrodes that remained in contact with air were neglected.

The parameter vector consisted of control points γ and conductivity of liquid σ_1 such that

$$\theta = (\gamma, \sigma_1)^{\mathrm{T}} \ .$$

The conductivity of air was approximated with a fixed small positive constant. The number of control points was four, that is $\gamma \in \mathbb{R}^8$. The air-liquid interface recovery was tested with two simulations.

Oil-water interface

In the oil-water interface reconstruction, the capacitive effects were taken into account. In this situation all electrodes could be used to inject and measure. The parameter vector consisted of control points γ, water conductivity σ_1 and the scaled permittivity coefficient of oil $\tilde{\epsilon}_0 = \omega\epsilon_{\mathrm{r}}\epsilon_0$ such that

$$\theta = (\gamma, \sigma_1, \tilde{\epsilon}_0)^{\mathrm{T}} \ .$$

The number of control points was four, that is, $\gamma \in \mathbb{R}^8$. The oil-water interface recovery was tested with two simulations.

Discussion

The results obtained from simulations are promising. It is suggested that the proposed approach could be used in the monitoring of industrial pipelines, for example, when the air-liquid or oil-water fraction inside the pipeline is of interest. The method recovered the admittivities and shapes of free-surfaces accurately.

In this method, the end points of the open surface were constrained to move along the domain boundary during iteration. This was carried out using Lagrangian constraints which prevented end points from moving off the domain boundary. Furthermore, proposed method avoided remeshing issues because the topology of the mesh was kept fixed during the iterations. If there are more than two flow regimes in the pipe, this method is extendable for monitoring those simultaneously.

One drawback of this method is that the reconstructions are presumably erroneous if there is a large inhomogeneity in the object domain and it is not taken into account. In practise, the simultaneous estimation of the shapes of inclusions with closed boundaries can be embedded to the proposed free-surface estimation method.

4.5.3 Sedimentation monitoring III–IV

The objective of this method is to recover the locations and velocities of phase interfaces in sedimentation processes. The motivation for the method stems from the

monitoring of sedimentation and other type of separation processes in industrial tanks.

The method uses the sedimentation model shown in Figure 2.2 and it is based on shape estimation techniques: Instead of using usual pixel based parameterization of EIT problem and post processing of the reconstructed pixel images, the EIT problem is parameterized directly with respect the locations (y-coordinates) of the phase interfaces (γ_1 and γ_2 in Figure 2.2) and the conductivities ($\sigma_1, \sigma_2, \sigma_3$) of the phase layers.

The problem of estimating the locations of the phase interfaces and phase conductivities is treated as a nonlinear state estimation problem within the framework of Section 4.3. By choosing the state estimation formulation, temporal evolution models for the heights of the phase interfaces and phase conductivities during the sedimentation can be embedded into the solution of the EIT problem.

Two-dimensional case III

In Publication III, a 2D model for the sedimentation monitoring is considered. The phase interfaces $\mathcal{C}_q(\gamma_q)$, $q = 1, 2$ are modelled as horizontal lines at the height γ_q (measured from the bottom of the tank).

The FEM implementation of the forward model $U(\theta)$ is similar to the method presented in Section 4.5.2. The main difference is that in the sedimentation monitoring two open interfaces have to be considered. Thus, the element classification procedure has to be done for three subregions instead of two. The evaluation of the integrals in equation (3.22) for the first-order basis functions is done with the aid of equations (4.34) and (4.35). In this case, there are three conductivity coefficients σ_k instead of two admittivity coefficients.

In Publication III, three different evolution models for the state parameters are considered. These models are random-walk, the first-order kinematic, and the second order-kinematic model. The advantage of the kinematic models is that the velocities of the phase interfaces are embedded as auxiliary parameters in the state. Thus, the velocity estimates are obtained directly as part of the state estimation process. The chosen kinematic models have been widely used in motion tracking problems [19, 85]. They are suitable models for parameters that change with nearly constant speed and acceleration between the measurement instants, respectively. In EIT, the kinematic models have been used, for example, in references [76, 77].

The computation of the Jacobian is carried out using equations (4.36) and (4.29).

The state estimation problem was solved using EKF equations (4.19–4.23). The performance of the proposed method and evolution models was tested with numerical simulations.

In the following, the employed evolution models are reviewed.

Random-walk

The simplest model for the evolution of the interfaces and the conductivities is the random-walk. In this model the locations of the interfaces (γ_1, γ_2) and the

values of the conductivities are assumed to be obtained from the previous state by adding white noise with the covariance Γ_{w_t}. In the component form the random walk model can be written as

$$\gamma_{t+1,i} = \gamma_{t,i} + w_{t,i} \ ,$$
$$\sigma_{t+1,j} = \sigma_{t,j} + w_{t,j} \ .$$

With the random walk model, the state parameter vector becomes

$$\theta_t = (\gamma_{t,1}, \gamma_{t,2}, \sigma_{t,1}, \sigma_{t,2}, \sigma_{t,3})^{\mathrm{T}} \ , \tag{4.38}$$

and the state transition matrices F_t and D_t in equation (4.16) become $F_t = D_t = I$, the identity matrix. In (4.38), $\gamma_{t,1}$ and $\gamma_{t,2}$ are the locations of the phase interfaces at time index t and $\sigma_{t,1}$,$\sigma_{t,2}$ and $\sigma_{t,3}$ are the conductivity values of the phase layers at time index t, respectively.

The first-order kinematic model

In the first-order kinematic model, the phase interfaces are assumed to move with nearly constant velocities between the consecutive measurement times (indices t and $t+1$). The componentwise evolution models for the location parameters $\gamma_{t,i},\ i = 1, 2$ become:

$$\gamma_{t+1,i} = \gamma_{t,i} + \dot{\gamma}_{t,i}\Delta T + \frac{1}{2}\Delta T^2 w_{t,i} \ , \tag{4.39}$$
$$\dot{\gamma}_{t+1,i} = \dot{\gamma}_{t,i} + \Delta T w_{t,i} \ , \tag{4.40}$$

where $\dot{\gamma}_{t,i}$ denotes the time derivative of the location of the interface (i.e., the settling velocity at time index t) and ΔT denotes the actual time difference between the time indices $t+1$ and t. In equations (4.39–4.40) the acceleration of the location of the interface is embedded into the state noise term, and the magnitude of the state noise covariance can be used to tune how much the dynamics are allowed to deviate from the constant speed movement. In the overall evolution model, similar first-order kinematic model, as in equations (4.39–4.40), is employed for the conductivity parameters $(\sigma_{t,1}, \sigma_{t,2}, \sigma_{t,3})$. With these choices, the parameter vector in (4.16) becomes

$$\theta_t = \left(\gamma_{t,1}, \dot{\gamma}_{t,1}, \gamma_{t,2}, \dot{\gamma}_{t,2}, \sigma_{t,1}, \dot{\sigma}_{t,1}, \sigma_{t,2}, \dot{\sigma}_{t,2}, \sigma_{t,3}, \dot{\sigma}_{t,3}\right)^{\mathrm{T}} \ ,$$

the state and noise transition matrices F_t and D_t become

$$F_t = \mathrm{blockdiag}\begin{pmatrix} 1 & \Delta T \\ 0 & 1 \end{pmatrix}, \quad D_t = \begin{pmatrix} \frac{1}{2}\Delta T^2 & 0 & 0 & \cdots \\ \Delta T & 0 & 0 & \cdots \\ 0 & \frac{1}{2}\Delta T^2 & 0 & \cdots \\ 0 & \Delta T & 0 & \cdots \\ \vdots & 0 & \ddots & \ddots \\ & \vdots & \ddots & \ddots \end{pmatrix} \ .$$

The second-order kinematic model

In the second-order kinematic model, the phase interfaces are assumed to move with nearly constant acceleration between the consecutive measurement times. The evolution model for the location parameters $\gamma_{t,i},\ i = 1, 2$ becomes

$$\gamma_{t+1,i} = \gamma_{t,i} + \dot{\gamma}_{t,i}\Delta T + \frac{1}{2}\ddot{\gamma}_{t,i}\Delta T^2 + \frac{1}{6}\Delta T^3 w_{t,i} \ , \tag{4.41}$$

$$\dot{\gamma}_{t+1,i} = \dot{\gamma}_{t,i} + \ddot{\gamma}_{t,i}\Delta T + \frac{1}{2}\Delta T^2 w_{t,i} \ , \tag{4.42}$$

$$\ddot{\gamma}_{t+1,i} = \ddot{\gamma}_{t,i} + \Delta T w_{t,i} \ , \tag{4.43}$$

where $\ddot{\gamma}_{t,i}$ denotes the second time derivative of the location of the interface (i.e., acceleration at time index t). In the overall evolution model, similar second-order kinematic model, as in equations (4.41–4.43), is employed for the conductivity parameters $(\sigma_{t,1}, \sigma_{t,2}, \sigma_{t,3})$. With these choices, the parameter vector in (4.16) becomes

$$\begin{aligned}\theta_t = (&\gamma_{t,1}, \dot{\gamma}_{t,1}, \ddot{\gamma}_{t,1}, \gamma_{t,2}, \dot{\gamma}_{t,2}, \ddot{\gamma}_{t,2}, \sigma_{t,1}, \dot{\sigma}_{t,1}, \ddot{\sigma}_{t,1},\\ &\sigma_{t,2}, \dot{\sigma}_{t,2}, \ddot{\sigma}_{t,2}, \sigma_{t,3}, \dot{\sigma}_{t,3}, \ddot{\sigma}_{t,3})^{\mathrm{T}} \ ,\end{aligned}$$

and the state and noise transition matrices become

$$F_t = \mathrm{blockdiag}\begin{pmatrix} 1 & \Delta T & \frac{1}{2}\Delta T^2 \\ 0 & 1 & \Delta T \\ 0 & 0 & 1 \end{pmatrix}, \quad D_t = \begin{pmatrix} \frac{1}{6}\Delta T^3 & 0 & 0 & \cdots & \\ \frac{1}{2}\Delta T^2 & 0 & 0 & \cdots & \\ \Delta T & 0 & 0 & \cdots & \\ 0 & \frac{1}{6}\Delta T^3 & 0 & \cdots & \\ 0 & \frac{1}{2}\Delta T^2 & 0 & \cdots & \\ 0 & \Delta T & 0 & \cdots & \\ \vdots & 0 & \ddots & \ddots & \\ & \vdots & & \ddots & \ddots \end{pmatrix} .$$

It is worth noting that the forward solution $U_t(\theta_t)$ does not depend explicitly on the first derivatives $\dot{\gamma}_{t,i}, \dot{\sigma}_{t,i}$ or the second derivatives $\ddot{\gamma}_{t,i}, \ddot{\sigma}_{t,i}$. When implementing the extended Kalman filter for the first and second order kinematic models, this is taken into account by simply adding zero columns to the Jacobian matrix J_t in equation (4.18) at the locations corresponding to the parameters $\dot{\gamma}_{t,i}$,$\dot{\sigma}_{t,i}$,$\ddot{\gamma}_{t,i}$ and $\ddot{\sigma}_{t,i}$.

Three-dimensional case IV

In Publication IV, the 2D approach for sedimentation monitoring is extended into 3D geometry. A new computational implementation of the forward model $U_t(\theta_t)$ is developed. The phase interfaces are assumed to be planes oriented along the xy -plane and the estimated parameters are the z-coordinates γ_q of these planes. Hence, the plane is of the form

$$\mathcal{C}_q(\gamma_q) = \{\mathsf{w} \in \mathbb{R}^3 | (\mathsf{w} - \mathsf{r_q})^{\mathrm{T}}\mathsf{n} = 0\} \ ,$$

where the normal vector of the plane is $\mathsf{n} = (0, 0, 1)^{\mathrm{T}}$ and the position vector is $\mathsf{r_q} = (0, 0, \gamma_q)^{\mathrm{T}}$. The phase interfaces (planes) are allowed to split the elements of the finite element mesh and thus no remeshing is needed. A three dimensional example of the element-interface splitting is illustrated in the Figure 4.4.

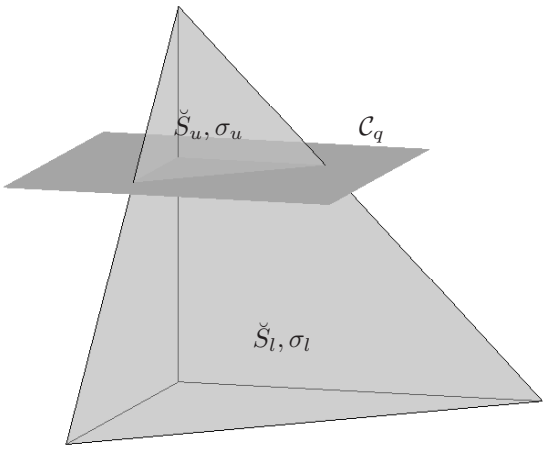

Figure 4.4: An example of a situation where the phase interface splits an element of the finite element mesh. In this situation one node of the element is on the upper side of the phase interface $\mathcal{C}_q$ and three nodes are on the lower side. $\breve{S}_u$ and $\breve{S}_l$ refer to the parts of the tetrahedrons which are on the upper and lower side of the phase interface $\mathcal{C}_q$, respectively.

The evaluation of the integrals in equation (3.22) is done with the aid of equations (4.34) and (4.35). In this case there are three conductivity coefficients σ_k instead of two admittivity coefficients. For the integration, the elements are divided into two classes:

- In the elements that are intercepted, the volume integrals of $\nabla\varphi_i \cdot \nabla\varphi_j$ have to be computed over parts of the FEM elements that belong to different phase layers, see Figure 4.4. In the case of the first-order (linear) basis the volume integral in (4.35) can alternatively be computed as a volume weighted average of the phase conductivities: Let Ω_m be an element divided into two parts by a phase interface as in Figure 4.4. By noting that the gradient of the first order basis functions φ_i, φ_j are constant over the whole element Ω_m,

the volume integration in (4.35) can be carried out as

$$\frac{\sigma_u|\breve{S}_u| + \sigma_l|\breve{S}_l|}{|\breve{S}_u| + |\breve{S}_l|} \int_{\Omega_m} \nabla\varphi_i \cdot \nabla\varphi_j \, \mathrm{d}r \;, \tag{4.44}$$

where $\breve{S}_u = \mathcal{S}_u \cap \Omega_m$, $\breve{S}_l = \mathcal{S}_l \cap \Omega_m$ and $\breve{S}_l \cup \breve{S}_u = \Omega_m$. $|\breve{S}_u|$ and $|\breve{S}_l|$ denote the volumes of the upper and lower parts of the split element. Here the subscripts u and l refer to the upper and lower side of the element Ω_m with respect to the intercepting phase interface, respectively. In the case of the first-order basis functions, the evaluation of integral in (4.44) is carried out as follows. It is noted that, the term $\nabla\varphi_i \cdot \nabla\varphi_j$ is constant and thus the integral can be written as

$$\int_{\Omega_m} \nabla\varphi_i \cdot \nabla\varphi_j \, \mathrm{d}r = c \int_{\Omega_m} \mathrm{d}r = c|\Omega_m| \;, \tag{4.45}$$

where c is constant.

- If the phase interface does not intersect the element, the volume-weighted average corresponds to the conductivity of the element. Furthermore, equation (4.45) can be used when computing the integrals.

The procedure is explained in detail in Publication IV.

In the computation of the Jacobian, the elements of the derivatives of the matrix A with respect to the interface locations are obtained as follows. Since the parameterization affects only to the B-block of the matrix A, only the term

$$\begin{aligned}\frac{\partial B(i,j)}{\partial\gamma_q} &= \frac{\partial}{\partial\gamma_q}\left(\sum_{k=1}^{3}\int_{\mathrm{supp}(\varphi_i\varphi_j)\cap\mathcal{S}_k} \sigma_k \nabla\varphi_i \cdot \nabla\varphi_j \, \mathrm{d}r\right) \\ &= \sum_{m|\Omega_m\in\mathcal{B}(\mathcal{C}_q)\cap\mathrm{supp}(\varphi_i\varphi_j)} \left[\frac{\partial}{\partial\gamma_q}\left(\frac{\sigma_u|\breve{S}_u| + \sigma_l|\breve{S}_l|}{|\breve{S}_u| + |\breve{S}_l|}\right)\int_{\Omega_m} \nabla\varphi_i \cdot \nabla\varphi_j \, \mathrm{d}r\right]\end{aligned}$$

needs to be computed. The element set $\mathcal{B}$ refers to the intersected elements. In Publication IV it is shown that the derivative in (4.44) can be written in the form

$$\frac{\partial B(i,j)}{\partial\gamma_q} = \frac{(\sigma_u - \sigma_l)}{|\Omega_m|}\frac{\partial|\breve{S}_u|}{\partial\gamma_q}\int_{\Omega_m} \nabla\varphi_i \cdot \nabla\varphi_j \, \mathrm{d}r \;. \tag{4.46}$$

Hence, the only derivative which needs to be computed for the evaluation of (4.46) is

$$\frac{\partial|\breve{S}_u|}{\partial\gamma_q} \;,$$

i.e., how the change in the interface location changes the volume of the upper subtetrahedron of the element Ω_m. The evaluation of the derivative $\partial|\breve{S}_u|/\partial\gamma_q$ is explained more specifically in Publication IV. The derivative with respect to the conductivities σ_k is computed as in (4.37).

The state estimation problem was solved using EKF equations (4.19–4.23). The performance of the proposed method and evolution models was tested with numerical simulations. The performance of the method proposed in Publication IV was tested with both simulated and experimental data. For the evolution of the phase interfaces the first-order kinematic model was used. The conductivities were assumed to be nearly constant and thus random-walk was employed for them.

Discussion

The results presented in Publications III and IV show that the developed sedimentation monitoring model performs well. The settling curves and velocity estimates obtained with kinematic models are accurate. The kinematic models are advantageous because the velocity estimates are obtained directly as a part of the state estimates. Thus, no post differentiation of the location estimates is needed.

The accuracy of the method is, however, presumably reduced if there are large local inhomogeneities in the phase layers. Based on the results, it is suggested that the proposed computational method can be used in the monitoring of sedimentation processes when knowledge of the locations and velocities of settling interfaces are of interest.

Chapter V

Summary and conclusions

In this thesis, shape estimation methods for electrical impedance tomography were developed. The motivation for the methods presented in this thesis stems from the industrial applications of EIT.

In Chapter 2, background of the thesis and motivation for the methods were discussed. The applications considered in this thesis were presented.

In Chapter 3, EIT was reviewed. More specifically, the mathematical model and its numerical solution using finite element method were discussed. Furthermore, electrical impedance tomography hardware used in this thesis was shortly reviewed.

In Chapter 4, the inverse problem of EIT was discussed. A brief review on the methods that have been applied to EIT inverse problem was given. Furthermore, the construction of the Jacobian matrix was discussed. The rest of Chapter 4 presented reviews of the shape estimation methods developed in the publications of this thesis.

The principal objectives in the shape estimation approaches were: to present a shape parameterization that is suitable for the considered practical application, and through the shape parameterization reduce the ill-posedness of the corresponding inverse problem. The different selections of parameterizations affected the FEM implementation of the forward problem. The corresponding inverse problem was stated as finding the shape parameters. Due to the nonlinearity of the inverse problem, the solution necessitated the computation of the Jacobian matrix. This was presented corresponding to the different FEM implementations.

Publication I

In this publication, a method for estimating the shape of the free-surface between air and conducting liquid in an industrial pipe was presented. The conducting liquid region was modelled using finite element mesh. The upper boundary of the object was assumed to represent the free-surface. The inverse problem was stated as a ROLS problem. The method was tested with simulated and experimental data. Based on the results it is concluded that the method is promising.

Publication II

The method in this publication was based on the assumption that the interior of the industrial pipe under investigation consists of two disjoint regions with different admittivities and these regions are separated with a smooth free-surface. The aim was then to estimate the shape of the free-surface and the corresponding permittivity coefficients of the regions. The inverse problem was stated as a ROLS problem augmented with two Lagrangian constraints. The constraints prevented the begin and end points of the free-surface from moving off the domain boundary. The performance of the method was tested with four numerical examples. From the results it can be seen that the method yields good estimates for the shape of the free-surface and admittivity coefficients.

Publication III

In this publication, a state estimation method for the monitoring of sedimentation processes using EIT was introduced. The aim of the method was to recover the time evolutions of the locations and velocities of the phase interfaces. The method assumed a piecewise constant three layer sedimentation model. Three different evolution models for the state estimation method were considered. The method was tested in numerical examples and evolution models were compared. From the results it is seen that the method performs well. Furthermore, the use of kinematic models can be seen to improve the estimates of the locations and velocities of the phase interfaces compared to the random-walk model.

Publication IV

The sedimentation monitoring method presented in Publication III was extended to three-dimensional geometry. The performance of the method was tested with the numerical simulation and experimental data. Based on the results it is seen that the method yields good estimates for the locations and velocities of the phase interfaces. Furthermore, the method exhibited a promising performance when experimental data were used.

Conclusions

The methods presented in this thesis are suggested to be used in industrial process monitoring. Furthermore, they provide a good computational framework for the further development of the shape estimation methods for industrial use. The methods have shown promising performance when tested with experimental and simulated data.

The free-surface estimation methods in Publications I and II were presented in 2D form. These free-surface estimation methods are extendable to 3D. Furthermore, when considering real industrial employment of the methods presented in this thesis, they should be improved such that they are less computationally demanding and adaptable to different industrial processes. One of the challenging tasks, especially, in the air-liquid interface estimation is the automatic detection

of the electrodes that are not in contact with conducting medium. One possible detection technique has been discussed for example in [16].

The methods developed in Publications I and II were developed using static assumptions. However, there are situations in which the target changes significantly faster compared to the time required to collect a full EIT data set. In these situations, the free-surface estimation problem can be formulated in the time-dependent state estimation form. This kind of implementation has been presented for two immiscible liquids in [78].

The sedimentation monitoring model developed in this thesis would be a potential method in industry when it is extended to monitor different types of separation processes. Furthermore, the issues regarding computational burden in 3D and accuracy of the models can be resolved by using the recently developed approximation error theory [71]. In the approximation error theory, for example, the errors due to the coarse discretization of models can be taken into account in the reconstruction. The use of optimal current patterns in sedimentation monitoring is also a future topic. The aim is to optimize the measurement paradigm based on a priori model of the target conductivity, see [69, 60].

Author's contribution

All publications are result of joint work with the supervisors and other co-authors. The author has been the principal writer in all the publications of this thesis. Furthermore, the author of this thesis carried out all the implementations of numerical methods, testing and computed the results in Matlab® platform. Some parts of the code for the forward problem have been adopted from the EIDORS package [117]. Furthermore, some parts of the element division code in Publications II and III are based on the previous work of supervisor in [80].

More specifically, in Publication I the author was responsible for the designing and implementation of the laboratory experiments, the construction, and modification of the tanks used in the laboratory experiments. Furthermore, the author implemented the numerical simulations. In Publication II, the author implemented FEM-calculations for the complex valued EIT with co-authors. Furthermore, the author implemented the inverse solver numerically. In Publication III, the author implemented numerically the forward and inverse solver. In Publication IV, the author implemented 3D finite element (forward and inverse) solver for the shape estimation problem and designed the specific sedimentation tank used in the laboratory experiments.

REFERENCES

[1] *Proc. of 1st European Concerted Action in Process Tomography (ECAPT) Workshop*, Manchester, UK, 1992.

[2] *Proc. of 2nd European Concerted Action in Process Tomography (ECAPT) Workshop*, Karlsruhe, Germany, 1993.

[3] *Proc. of 3rd European Concerted Action in Process Tomography (ECAPT) Workshop*, Oporto, Portugal, 1994.

[4] *Proc. of 4th European Concerted Action in Process Tomography (ECAPT) Workshop*, Bergen, Norway, 1995.

[5] *Proc. of 1st World Congress in Industrial Process Tomography*, Buxton, UK, 1999.

[6] *Proc. of 2nd World Congress in Industrial Process Tomography*, Hannover, Germany, 2001.

[7] *Proc. of 3rd World Congress in Industrial Process Tomography*, Banff, Canada, 2003.

[8] *Proc. of 4th World Congress in Industrial Process Tomography*, Aizu, Japan, 2005.

[9] W.H. Ahmed. Capacitance sensors for void-fraction measurements and flow-pattern indentification in air-oil two-phase flow. *IEEE Sens J*, 6:1153–1163, 2006.

[10] G. Alessandrini and L. Rondi. Stable determination of a crack in a planar inhomogeneous conductor. *SIAM J Appl Math*, 30(2):326–340, 1998.

[11] B.D.O. Anderson and J.B. Moore. *Optimal filtering*. Prentice-Hall, inc, 1979.

[12] W. Annicchiarico and M. Cerrolaza. Finite elements, genetic algorithms and β-splines: a combined technique for shape optimization. *Finite Elem Anal Des*, 33:125–141, 1999.

[13] W. Annicchiarico and M. Cerrolaza. Structural shape optimization 3D finite-element models based on genetic algorithms and geometric modeling. *Finite Elem Anal Des*, 37:403–415, 2001.

[14] N.D. Aparicio and M.K. Pidcock. The boundary inverse problem for the Laplace equation in two dimensions. *Inverse Probl*, 12:565–577, 1996.

[15] S.R. Arridge. Optical tomography in medical imaging. *Inverse Probl*, 15:R41–R93, 1999.

[16] Y. Asfaw and A. Adler. Automatic detection of detached and erroneous electrodes in electrical impedance tomography. *Physiol Meas*, 26:S175–S183, 2005.

[17] K. Astala and L. Päivärinta. Calderóns inverse conductivity problem in the plane. *Ann of Math*, 163:265–299, 2006.

[18] S. Babaeizadeh, D.H. Brooks, and D. Isaacson. A deformable-radius B-spline

method for shape-based inverse problems, as applied to electrical impedance tomography. In *IEEE International Conference on Acoustics, Speech, and Signal Processing*, volume 2, pages 485–488, March 18-23 2005.

[19] Y. Bar-Shalom and X.R. Li. *Estimation and Tracking: Principles, Techniques, and Softwares*. Artech House, 1993.

[20] D.C. Barber and B.H. Brown. Applied potential tomography. *J Phys E: Sci Instrum*, 17:723–733, 1984.

[21] D. Barnea. A unified model for predicting flow-pattern transitions for the whole range of pipe inclinations. *Int J Multiphas Flow*, 13:1–12, 1987.

[22] A.T. Batayneh and A.A. Al-Diabat. Application of a two-dimensional electrical tomography technique for investigating landslides along the Amman–Dead Sea highway, Jordan. *Environ Geol*, 42:399–403, 2002.

[23] E. Beretta and S. Vessella. Stable determination of boundaries from Cauchy data. *SIAM J Appl Math*, 30(1):220–232, 1998.

[24] J. Blewett, W.J. McCarter, T.M. Chrisp, and G. Starrs. Monitoring sedimentation of a clay slurry. *Géotechnique*, 51:723–728, 2001.

[25] B.H. Blott, G.J. Daniell, and S. Meeson. Nonlinear reconstruction constrained by image properties in electrical impedance tomography. *Phys Med Biol*, 43:1215–1224, 1998.

[26] G.T. Bolton, C.H. Qiu, and M. Wang. A novel electrical tomography sensor for monitoring the phase distribution in industrial reactors. In *7th UK Conference on Mixing*, Bradford, UK, 2002.

[27] W.R. Breckon and M.K. Pidcock. Mathematical aspects of impedance imaging. *Clin Phys Physiol Meas, Suppl A*, 8:77–84, 1987.

[28] B.H. Brown, D.C. Barber, and A.D. Seagar. Applied potential tomography: possible clinical applications. *Clin Phys Physiol Meas*, 6:109–121, 1985.

[29] R. Bürger, S. Evje, K.H. Karlsen, and K.-A. Lie. Numerical methods for the simulation of the settling of flocculated suspensions. *Chem Eng J*, 80:91–104, 2000.

[30] R. Bürger and W.L. Wendland. Sedimentation and suspension flows: Historical perspective and some recent developments. *J Eng Math*, 41:101–116, 2001.

[31] J.E. Butler and R.T. Bonnecaze. Inverse method for imaging a free surface using electrical impedance tomography. *Chem Eng Sci*, 55:1193–1204, 2000.

[32] A.P. Calderón. On an inverse problem boundary value problem. In W.H. Meyer and M.A. Raupp, editors, *Seminar on Numerical Analysis and its Applications to Continuum Physics*, pages 65–73. Brazilian Math. Society, Rio de Janeiro, 1980.

[33] T.F. Chan and X.-C. Tai. Level set and total variation regularization for elliptic inverse problems with discontinuous coefficients. *J Comput Phys*, 193(1):40–66, 2004.

[34] M. Cheney and D. Isaacson. Distinguishability in impedance imaging. *IEEE Trans Biomed Eng*, 39:852–860, 1992.

[35] K.-S. Cheng, D. Isaacson, J.C. Newell, and D.G. Gisser. Electrode models for electric current computed tomography. *IEEE Trans Biomed Eng*, 36:918–924, 1989.

[36] K.-S. Cheng, S.J. Simske, D. Isaacson, J.C. Newell, and D.G. Gisser. Errors due to measuring voltage on current-carrying electrodes in electric current computed tomography. *IEEE Trans Biomed Eng*, 37:60–65, 1990.

[37] C. Colin and J. Fabre. Gas-liquid pipe flow under microgravity conditions: influence of tube diameter on flow patterns and pressure drops. *Adv Space Res*, 16:137–142, 1995.

[38] R.D. Cook, G.J. Saulnier, D.G. Gisser, J.C. Goble, J.C. Newell, and D. Isaacson. Act3: A high-speed, high precision electrical impedance tomography. *IEEE Trans Biomed Eng*, 41:713–722, 1994.

[39] J.C. Cullivan, M. Wang, G. Bolton, G. Baker, W. Clark, and R.A. Williams. Linear EIT for sedimentation and sediment bed characterization. In *Proceedings of 4th World Congress on Industrial Process Tomography*, pages 910–915, Aizu, Japan, 5.-8.9. 2005. The Virtual Centre for Industrial Process Tomography.

[40] K.R. Demarest. *Engineering Electromagnetics*. Prentice Hall, New Jersey, 1998.

[41] F. Dong, X. Liu, X. Deng, L. Xu, and L.A. Xu. Identification of two-phase flow regimes in horizontal, inclined and vertical pipes. *Meas Sci Technol*, 12:1069–1075, 2001.

[42] F. Dong, X.T. Qiao, Z.X. Jiang, and L.A. Xu. Application of electrical resistance tomography to two-phase flow and void fraction measurement. In *Proceedings of 3rd World Congress on Industrial Process Tomography*, pages 299–304, Banff, Canada, 2.-5.9. 2003. The Virtual Centre for Industrial Process Tomography.

[43] P.M. Edic, D. Isaacson, G.J. Saulnier, H. Jain, and J.C. Newell. An iterative Newton-Rhapson method to solve the inverse admittivity problem. *IEEE Trans Biomed Eng*, 45:899–908, 1998.

[44] Y.V. Fairuzov, P. Arenas-Medina, J. Verdejo-Fierro, and R. Gonzales-Islas. Flow pattern transitions in horizontal pipelines carrying oil-water mixtures: full-scale experiments. *J Energ Resour-ASME*, 122:169–176, 2000.

[45] G. Fehmers. Volumetric flow rates from impedance tomography in oil/gas flows. In *Proceedings of 3rd World Congress on Industrial Process Tomography*, pages 287–292, Banff, Canada, 2.-5.9. 2003. The Virtual Centre for Industrial Process Tomography.

[46] L. Freitag. On combining laplacian and optimization-based mesh smoothing techniques, 1997.

[47] D.G. Gisser, D. Isaacson, and J.C. Newell. Electric current computed tomography and eigenvalues. *SIAM J Appl Math*, 50:1623–1634, 1990.

[48] J. Haslinger and R.A.E. Mäkinen. *Introduction to shape optimization : theory, approximation, and computation*. SIAM, Philadelphia, 2003.

[49] J. Haslinger and P. Neittaanmäki. *Finite element approximation for optimal shape design*. John Wiley & Sons, Chichester, 1988.

[50] L.M. Heikkinen. *Statistical estimation methods for electrical process tomography*. PhD thesis, University of Kuopio, Finland, 2005.

[51] L.M. Heikkinen, J. Kourunen, T. Savolainen, P.J. Vauhkonen, J.P. Kaipio, and M. Vauhkonen. Real time three-dimensional electrical impedance tomography applied in multiphase flow imaging. *Meas Sci Technol*, 17:2083–2087, 2006.

[52] L.M. Heikkinen, T. Vilhunen, R.M. West, and M. Vauhkonen. Simultaneous reconstruction of electrode contact impedances and internal electrical properties: II. laboratory experiments. *Meas Sci Technol*, 13:1855–1861, 2002.

[53] J. Heino. Approaches for modelling and reconstruction in optical tomography in the presence of anisotropies. Doctoral dissertation, Helsinki University of Technology, 2005.

[54] J. Heino, E. Somersalo, and J.P. Kaipio. Compensation for geometric mismodelling by anisotropies in optical tomography. *Opt Express*, 13:296–308, 2005.

[55] R.P. Henderson and J.G. Webster. An impedance camera for spatially specific measurements of the thorax. *IEEE Trans Biomed Eng*, 25:250–254, 1978.

[56] F. Hettlich and W. Rundell. Iterative methods for the reconstruction of an inverse

potential problem. *Inverse Probl*, 12:251–266, 1996.

[57] E. Hinton and D.R.J. Owen. *An introduction to finite element computations*. Pineridge Press Limited, Swansea, U.K., 1979.

[58] P. Hua, J.G. Webster, and W.J. Tompkins. A regularized electrical impedance tomography reconstruction algortihm. *Clin Phys Physiol Meas, Suppl A*, 9:137–141, 1988.

[59] P. Hua, E.J. Woo, J.G. Webster, and W.J. Tompkins. Iterative reconstruction methods using regularization and optimal current patterns in electrical impedance tomography. *IEEE Trans Med Imaging*, 10:621–628, 1991.

[60] D. Isaacson. Distinguishability of conductivities by electric current computed tomography. *IEEE Trans Med Imaging*, 5:91–95, 1986.

[61] I. Ismail, J.C. Gamio, S.F.A. Bukhari, and W.Q. Yang. Tomography for multiphase flow measurement in the oil industry. *Flow Meas Instrum*, 16:145–155, 2005.

[62] Industrial tomography systems, ITS. http://www.itoms.com.

[63] A.J. Jaworski and T. Dyakowski. Application of electrical capacitance tomography for measurement of gas-solids flow characteristics in a pneumatic conveying system. *Meas Sci Technol*, 12:1109–1119, 2001.

[64] A.J. Jaworski and T. Dyakowski. Measurements of oil–water separation dynamics in primary separation systems using distributed capacitance sensors. *Flow Meas Instrum*, 16:113–127, 2005.

[65] O.C. Jones and N. Zuber. The interrelation between void fraction fluctuations and flow patterns in two-phase flow. *Int J Multiphas Flow*, 2:273–306, 1975.

[66] J. Jordana, M. Gasulla, and R. Pallàs-Areny. Electrical resistance tomography to detect leaks from buried pipes. *Meas Sci Technol*, 12:1061–1068, 2001.

[67] Y. Kagawa, W. Xu, Y. Zhao, N. Wakatsuki, and H. Totsuji. Electrical impedance ground prospecting for anomaly detection using direct inversion algorithm with dual reciprocity boundary element modeling. In *Inverse Problems, Design and Optimization Symposium*, Rio de Janeiro, Brazil, 2004.

[68] J.P. Kaipio, P.A. Karjalainen, E. Somersalo, and M. Vauhkonen. State estimation in time-varying electrical impedance tomography. *Ann NY Acad Sci*, 873:430–439, 1999.

[69] J.P. Kaipio, A. Seppänen, E. Somersalo, and H. Haario. Posterior covariance related optimal current patterns in electrical impedance tomography. *Inverse Probl*, 20:919–936, 2004.

[70] J.P. Kaipio and E. Somersalo. Nonstationary inverse problems and state estimation. *J Inverse Ill Posed Probl*, 7:273–282, 1999.

[71] J.P. Kaipio and E. Somersalo. *Statistical and Computational Inverse Problems*, volume 160 of *Applied Mathematical Sciences*. Springer-Verlag, New York, 2004.

[72] H. Kang, J.K. Seo, and D. Sheen. Numerical identification of discontinuous conductivity coefficients. *Inverse Probl*, 13:113–123, 1997.

[73] T.-J. Kao, J.C. Newell, G.J. Saulnier, and D. Isaacson. Distinguishability of inhomogeneities using planar electrode arrays and different patterns of applied excitation. *Physiol Meas*, 24:403–411, 2004.

[74] A. Kemna, J. Vanderborght, B. Kulessa, and H. Vereecken. Imaging and characterization of sub sufrace solute transport using electrical resistivity tomography (ert) and equivalent transport models. *J Hydrol*, 267:125–146, 2002.

[75] B.S. Kim, U.Z. Ijaz, J.H. Kim, M.C. Kim, S. Kim, and K.Y. Kim. Nonstationary phase boundary estimation in electrical impedance tomography based on the interacting multiple model scheme. *Meas Sci Technol*, 18:62–70, 2007.

[76] K.Y. Kim, B.S. Kim, M.C. Kim, and S. Kim. Dynamic inverse obstacle problems with electrical impedance tomography. *Math Comput Simulat*, 66:399–408, 2004.

[77] K.Y. Kim, B.S. Kim, M.C. Kim, S. Kim, D. Isaacson, and J.C. Newell. Dynamical electrical impedance imaging with the interacting multiple model scheme. *Physiol Meas*, 26:S217–S233, 2005.

[78] S. Kim, U.Z. Ijaz, A.K. Khambampati, K.Y. Kim, M.C. Kim, and S.I. Chung. Moving interfacial boundary estimation in stratified flow of two immiscible liquids using electrical resistance tomography. *Meas Sci Technol*, 18:1257–1269, 2007.

[79] V. Kolehmainen. *Novel approaches to image reconstruction in diffusion tomography*. PhD thesis, University of Kuopio, Kuopio, Finland, 2001.

[80] V. Kolehmainen, S.R. Arridge, W.R.B Lionheart, and M. Vauhkonen. Recovery of region boundaries of piecewise constant coefficients of an elliptic PDE from boundary data. *Inverse Probl*, 15:1375–1391, 1999.

[81] V. Kolehmainen, S.R. Arridge, M. Vauhkonen, and J.P. Kaipio. Simultaneous reconstruction of internal tissue region boundaries and coefficients in optical diffusion tomography. *Phys Med Biol*, 45:3267–3283, 2000.

[82] V. Kolehmainen, M. Lassas, and P. Ola. On the inverse conductivity problem with an imperfectly known boundary. *SIAM J Appl Math*, 66:365–383, 2005.

[83] V. Kolehmainen, A. Voutilainen, and J.P. Kaipio. Estimation of nonstationary region boundaries in EIT – state estimation approach. *Inverse Probl*, 17:1937–1956, 2001.

[84] J. Kourunen, T. Savolainen, L.M. Heikkinen, A. Lehikoinen, and M. Vauhkonen. Novel impedance tomography system for industrial use. Manuscript in preparation.

[85] X. Rong Li. Canonical transform for tracking with kinematic models. *IEEE Trans Aerospace and Electronic Systems*, 33:1212–1224, 1997.

[86] E. Lund, H. Møller, and L.A. Jakobsen. Shape design optimization of steady fluid-structure interaction problems with large displacements. *American Institute of Aeronautics and Astronautics Paper 2001-1624*, 2001.

[87] A.D. Martin. Optimisation of clarifier-thickeners processing stable suspensions for turn-up/turn-down. *Water Res*, 38:1568–1578, 2004.

[88] F.J. McArdle, B.H. Brown, R.G. Pearse, and D.C. Barber. The effect of the skull of low-birthweight neonates on applied potential tomography imaging of centralised resistivity changes. *Clin Phys Physiol Meas, Suppl A*, 9:55–69, 1988.

[89] J. Mueller and S. Siltanen. Direct reconstructions of conductivities from boundary measurements. *SIAM J Sci Comput*, 24:1232–1266, 2003.

[90] D. Murphy, P. Burton, R. Coombs, L. Tarassenko, and P. Rolfe. Impedance imaging in the newborn. *Clin Phys Physiol Meas, Suppl A*, 8:131–140, 1987.

[91] S.C. Murphy, S.J. Stanley, D. Rhodes, and T.A. York. 3D electrical tomographic imaging using vertical arrays of electrodes. *Meas Sci Technol*, 17:3053–3065, 2006.

[92] A.I. Nachman. Global uniqueness for a two-dimensional inverse boundary value problem. *Ann of Math*, 143:71–96, 1996.

[93] D. Neuffer, A. Alvarez, D.H. Owens abd K.L. Ostorowski, S.P. Luke, and R.A. Williams. Control of pneumatic conveying using ECT. In *Proceedings of 1st World Congress on Industrial Process Tomography*, pages 71–77, Buxton, UK, 1999. The Virtual Centre for Industrial Process Tomography.

[94] J. Nocedal and S.J. Wright. *Numerical Optimization*. Springer Series in Operations Research. Springer-Verlag, New York, 1999.

[95] A.D. Pachowko, M. Wang, C. Poole, and D. Rhodes. The use of electrical resistance tomography (ERT) to monitor flow patterns in horizontal slurry transport

pipelines. In *Proceedings of 3rd World Congress on Industrial Process Tomography*, pages 305–311, Banff, Canada, 2.-5.9. 2003. The Virtual Centre for Industrial Process Tomography.

[96] K. Paulson, W. Lionheart, and M. Pidcock. POMPUS: an optimized EIT reconstruction algorithm. *Inverse Probl*, 11:425–437, 1995.

[97] D. Pinelli, G. Montante, and F. Magelli. Dispersion coefficients and settling velocities of solids in slurry vessels stirred with different types of multiple impellers. *Chem Eng Sci*, 59:3081–3089, 2004.

[98] M.A. Player, J. van Weereld, J.M.S. Hutchison, A.R. Allen, and L. Shang. An electrical impedance tomography algorithm with well–defined spectral properties. *Meas Sci Technol*, 10:L9–L14, 1999.

[99] K. Primrose and C. Qiu. Electrical impedance tomographic sensor systems. *Sensor Review*, 20:189–195, 2000.

[100] K.S. Rezkallah and L. Zhao. Flow pattern map for two-phase liquid-gas flows under reduced gravity conditions. *Adv Space Res*, 16:133–136, 1995.

[101] F. Ricard, C. Brechtelsauber, X.Y. Xu, and C.J. Lawrence. Monitoring of multiphase pharmaceutical processes using electrical resistance tomography. *Trans IChemE, Part A, Chem Eng Res Des*, 83:794–805, 2005.

[102] D.F. Rogers. *An Introduction to NURBS With Historical Perspective*. Morgan Kaufmann Publishers, San Francisco, 2001.

[103] F. Santosa and M. Vogelius. A backprojection algorithm for electrical impedance imaging. *SIAM J Appl Math*, 50:216–243, 1990.

[104] T. Savolainen, L.M. Heikkinen, M. Vauhkonen, and J.P. Kaipio. A modular, adaptive electrical impedance tomography system. In *Proceedings of 3rd World Congress on Industrial Process Tomography*, pages 50–55, Banff, Canada, 2.-5.9. 2003. The Virtual Centre for Industrial Process Tomography.

[105] M. Schweiger, S.R. Arridge, and I. Nissilä. Gauss–Newton method for image reconstruction in diffuse optical tomography. *Phys Med Biol*, 50:2365–2386, 2005.

[106] A. Seppänen. *State estimation in process tomography*. PhD thesis, University of Kuopio, Finland, 2005.

[107] A. Seppänen, M. Vauhkonen, P.J. Vauhkonen, E. Somersalo, and J.P. Kaipio. State estimation with fluid dynamical evolution models in process tomography – an application to impedance tomography. *Inverse Probl*, 17:467–484, 2001.

[108] S.P. Sharma and V.C. Baranwal. Delineation of groundwater-bearing fracture zones in a hard rock area integrating very low frequency electromagnetic and resistivity data. *J Appl Geophys*, 57:155–166, 2005.

[109] S. Siltanen, J. Mueller, and D. Isaacson. An implementation of the reconstruction algorithm of A. Nachman for the 2-D inverse conductivity problem. *Inverse Probl*, 16:681–699, 2000.

[110] R.M.W. Smith, I.L. Freeston, and B.H. Brown. A real time electrical impedance tomography system for clinical use – design and preliminary results. *IEEE Trans Biomed Eng*, 42:133–140, 1995.

[111] E. Somersalo, M. Cheney, and D. Isaacson. Existence and uniqueness for electrode models for electric current computed tomography. *SIAM J Appl Math*, 52:1023–1040, 1992.

[112] J. Sylvester and G. Uhlmann. A global uniqueness theorem for an inverse boundaty value problem. *Ann of Math*, 125:153–169, 1987.

[113] L.H. Tsoukalas, M. Ishii, and Y. Mi. A neurofuzzy methodology for impedance-based multiphase flow identification. *Engng Applic Artif Intell*, 10:545–555, 1997.

[114] A. Uribe-Salas, C.O. Gomez, and J.A. Finch. A conductivity technique for gas and solids holdup determination in three-phase reactors. *Chem Eng Sci*, 49:1–150, 1994.

[115] M. Vauhkonen. *Electrical impedance tomography and prior information*. PhD thesis, University of Kuopio, Kuopio, Finland, 1997.

[116] M. Vauhkonen, P.A. Karjalainen, and J.P. Kaipio. A Kalman filter approach to track fast impedance changes in electrical impedance tomography. *IEEE Trans Biomed Eng*, 45:486–493, 1998.

[117] M. Vauhkonen, W.R.B. Lionheart, L.M. Heikkinen, P.J. Vauhkonen, and J.P. Kaipio. A MATLAB package for the EIDORS project to reconstruct two-dimensional EIT images. *Physiol Meas*, 22:107–111, 2001.

[118] M. Vauhkonen, D. Vadász, P.A. Karjalainen, E. Somersalo, and J.P. Kaipio. Tikhonov regularization and prior information in electrical impedance tomography. *IEEE Trans Med Imaging*, 17:285–293, 1998.

[119] P.J. Vauhkonen. *Image reconstruction in three-dimensional electrical impedance tomography*. PhD thesis, University of Kuopio, Kuopio, Finland, 2004.

[120] P.J. Vauhkonen, M. Vauhkonen, and J.P. Kaipio. Fixed-lag smoothing and state estimation in dynamic electrical impedance tomography. *Int J Numer Meth Engng*, 50:2195–2209, 2001.

[121] J.M. Vergouw, J. Anson, R. Dalhke, Z. Xu, C. Gomez, and J.A. Finch. An automated data acquistion technique for settling tests. *Miner Eng*, 10:1095–1105, 1997.

[122] T. Vilhunen, J.P. Kaipio, P.J. Vauhkonen, T. Savolainen, and M. Vauhkonen. Simultaneous reconstruction of electrode contact impedances and internal electrical properties: I. theory. *Meas Sci Technol*, 13:1848–1854, 2002.

[123] J.G. Webster. *Electrical Impedance Tomography*. Adam Hilger, Bristol, UK, 1990.

[124] D.A. White and N. Verdone. Numerical modelling of sedimentation processes. *Chem Eng Sci*, 55:2213–2222, 2002.

[125] E.J. Woo, P. Hua, J.G. Webster, and W.J. Tompkins. A robust image reconstruction algorithm and its parallel implementation in electrical impedance tomography. *IEEE Trans Med Imaging*, 12:137–146, 1993.

[126] C.G. Xie, N. Reinecke, M.S. Beck, D. Mewes, and R.A. Williams. Electrical tomography techniques for process engineering applications. *Chem Eng J*, 56:127–133, 1995.

[127] T.A. York. Status of electrical tomography in industrial applications. *J Electron Imag*, 10:608–619, 2001.

[128] T.J. Yorkey, J.G. Webster, and W.J. Tompkins. Comparing reconstruction algorithms for electrical impedance tomography. *IEEE Trans Biomed Eng*, 34:843–852, 1987.

[129] H. Yoshida, T. Nurtono, and K. Fukui. A new method for the control of dilute suspension sedimentation by horizontal movement. *Powder Technol*, 150:9–19, 2005.

[130] Y. Zhu, J. Wu, I.S. Shepherd, M. Coghill, N. Vagias, and K. Elkin. An automated measurement technique for slurry settling tests. *Miner Eng*, 13:765–772, 2000.

Kuopio University Publications C. Natural and Environmental Sciences

C 196. Heijari, Juha. Seed origin, forest fertilization and chemical elicitor influencing wood characteristics and biotic resistance of Scots pine.
2006. 39 p. Acad. Diss.

C 197. Hakulinen, Mikko. Prediction of density, structure and mechanical properties of trabecular bone using ultrasound and X-ray techniques.
2006. 84 p. Acad. Diss.

C 198. Al Natsheh, Anas. Quantum Mechanics Study of Molecular Clusters Composed of Atmospheric Nucleation Precursors.
2006. 55 p. Acad. Diss.

C 199. Tarvainen, Tanja. Computational Methods for Light Transport in Optical Tomography.
2006. 123 p. Acad. Diss.

C 200. Heikkinen, Päivi. Studies on Cancer-related Effects of Radiofrequency Electromagnetic Fields. 2006. 165 p. Acad. Diss.

C 201. Laatikainen, Tarja. Pesticide induced responses in ectomycorrhizal fungi and symbiont Scots pine seedlings.
2006. 180 p. Acad. Diss.

C 202. Tiitta, Markku. Non-destructive methods for characterisation of wood material.
2006. 70 p. Acad. Diss.

C 203. Lehesranta, Satu. Proteomics in the Detection of Unintended Effects in Genetically Modified Crop Plants.
2006. 71 p. Acad. Diss.

C 204. Boman, Eeva. Radiotherapy forward and inverse problem applying Boltzmann transport equation.
2007. 138 p. Acad. Diss.

C 205. Saarakkala, Simo. Pre-Clinical Ultrasound Diagnostics of Articular Cartilage and Subchondral Bone.
2007. 96 p. Acad. Diss.

C 206. Korhonen, Samuli-Petrus. FLUFF-BALL, a Fuzzy Superposition and QSAR Technique - Towards an Automated Computational Detection of Biologically Active Compounds Using Multivariate Methods.
2007. 154 p. Acad. Diss.

C 207. Matilainen, Merja. Identification and characterization of target genes of the nuclear reseptors VDR and PPARs: implementing in silico methods into the analysis of nuclear receptor regulomes.
2007. 112 p. Acad. Diss.

C 208. Anttonen, Mikko J. Evaluation of Means to Increase the Content of Bioactive Phenolic Compounds in Soft Fruits.
2007. 93 p. Acad. Diss.

C 209. Pirkanniemi, Kari. Complexing agents: a study of short term toxicity, catalytic oxidative degradation and concentrations in industrial waste waters.
2007. 83 p. Acad. Diss.

C 210. Leppänen, Teemu. Effect of fiber orientation on cockling of paper.
2007. 96 p. Acad. Diss.